Insights into the North Patagonian Massif lower crust: petrology and microstructure of granulite xenoliths

Noé Muckensturm, Mary-Alix Kaczmarek, Michel Grégoire, Theodoros Ntaflos, Ernesto Bjerg, Frédéric Mouthereau

Insights into the North Patagonian Massif lower crust: petrology and microstructure of granulite xenoliths.

Noé Muckensturm[1]*, Mary-Alix Kaczmarek[1], Michel Grégoire[1], Theodoros Ntaflos[2], Ernesto A. Bjerg[3] and Fréderic Mouthereau[1]

[1]Géosciences Environnement Toulouse, UPS-CNRS-CNES-IRD, OMP 14 Avenue E. Belin, 31400 Toulouse, France

[2]University of Vienna, Department of Lithospheric Research, Josef-Holaubek-Platz 2, 1090 Wien, Austria

[3]Instituto Geológico del Sur (INGEOSUR, UNS-CONICET), Departamento de Geología, Universidad Nacional del Sur, San Juan 670, 8000, Bahía Blanca, Buenos Aires, Argentina

* Corresponding author. Telephone : (+33) 638680157. E-mail: noe.muckensturm@outlook.com

ABSTRACT

The continental lower crust constitutes a key zone for understanding the mantle-crust magmatic and mechanical transfers, but its study is hampered by the paucity of lower crust samples. Here, we characterise the petrological, geochemical and petrophysical processes structuring the lower crust of the North Patagonian Massif (NPM; Argentina) using a suite of representative mafic granulite and websterite xenoliths. These xenoliths were entrained by alkaline lavas from 5 volcanic centres that erupted between the Oligocene and Pleistocene. Electron microprobe and laser ablation inductively coupled plasma mass spectrometer (LA-ICPMS) were used to obtain in-situ geochemical data on the minerals, while microstructural data were obtained by Electron Backscatter Diffraction (EBSD). Both granulites and

websterites display a granoblastic texture and sometimes a weak inherited magmatic layering. Mafic granulite xenoliths show a plagioclase + clinopyroxene ± orthopyroxene assemblage commonly associated with spinel or titanomagnetite. Websterite xenoliths show an association of clinopyroxene + orthopyroxene + spinel, along with accessory plagioclase. Mafic granulites and websterites have SiO_2 contents ranging from 44 to 53 wt% while their Mg# varies from 53 to 79. Clinopyroxenes are characterised by weak convex upward chondrite-normalised Rare Earth Elements - REE patterns (Light-REE </<< Mid-REE > Heavy-REE) which are similar to clinopyroxene phenocrysts and megacrysts from intra-plate basalts. Calculated liquid in equilibrium with clinopyroxene have similar REE patterns to those found in Cenozoic basalts from the NPM, suggesting that the xenolith suite represents evidence for underplating processes, possibly related to one of the magmatic events that have occured in the NPM since the Permo-Trias. Mafic granulites and websterites show a weak mineral shape preferred orientation and an associated weak crystal preferred orientation (CPO) related to the magmatic layering. Recorded plastic deformation is associated with the activation of both (100)[001] and (001)[100] slip systems in clinopyroxene, (100)[001] in orthopyroxene and (010)[001] in plagioclase. However, the activation of slip systems is generally not correlated with CPO in granulites, suggesting that the lower crust underwent subsolidus equilibration and weak plastic deformation in an inactive tectonic context, thereby preserving an inherited magmatic layering. Two-pyroxene (Fe-Mg) thermometer and pseudosection calculations define P-T conditions of the main paragenesis at 760-1120°C and

7.2-10.3 kbar, which allows to define the Cenozoic geotherm of the NPM crust at 30°C/km and to reconsider the petrologic Moho depth at ca. 40 km.

Keywords: Xenoliths, mafic granulites, microstructure, thermobarometry, trace elements, Patagonia

INTRODUCTION

The debate on the constitution and structuring of the continental lower crust, and its transition to the mantle, is still ongoing. The lower crust is an important zone for understanding the complex processes of crust-mantle transfers. These transfers can be magmatic in nature, with magma underplating, associated magma fractionation and assimilation, or lithospheric delamination (Cawood *et al.*, 2013, 2022; Gianni & Navarrete, 2022) and mechanical, with the transfer of plate tectonic strain into the crust via decoupling processes at the crust-mantle boundary (Coltice *et al.*, 2019; Mouthereau *et al.*, 2021). However, understanding the effects of these transfers on the structure of the continental lower crust is challenging for two main reasons: the lower crust is rarely exposed at the Earth's surface, and existing knowledge is mainly derived from xenoliths studies, which do not provide spatial resolution (Mengel & Kern, 1992; Rudnick & Fountain, 1995; O'Reilly & Griffin, 2013; Hacker *et al.*, 2015).

The North Patagonian Massif (NPM; Rio Negro Province, Argentina) lacks outcrops of mid-to-lower crustal rock (e.g. Rapela & Pankhurst, 2020), so the nature of its lower crust remains controversial. While the oldest exposed rocks in the massif are igneous and metasedimentary Early Paleozoic (Early Cambrian to Silurian), the age of the basement has been indirectly inferred as Mesoproterozoic (1200-1000 Ma) from U-Pb ages of detrital zircons (Pankhurst *et al.*, 2006; Rapalini *et al.*, 2013), from U-Pb ages and Hf model ages of inherited metamorphic and magmatic zircon cores (Rapalini *et al.*, 2013; Pankhurst *et al.*,

2014; Rapela & Pankhurst, 2020), and from whole-rock Nd model ages of Paleozoic igneous rocks (Martínez Dopico *et al.*, 2011; Pankhurst *et al.*, 2014). The NPM Mesoproterozoic lower crust of the NPM has a refractory character based on the geochemical study of xenoliths from the Sierra de los Chacays (Southern NPM, Pankhurst & Rapela, 1995). It recorded crustal anatexis, magmatic remobilisation between the Devonian (Late Paleozoic) and the Jurassic (Pankhurst & Rapela, 1995; Pankhurst *et al.*, 1998; Pankhurst *et al.*, 2006; Luppo *et al.*, 2018; Zaffarana *et al.*, 2020; Falco *et al.*, 2022; Gianni & Navarrete, 2022, Oriolo *et al.*, 2023). These studies of the NPM lower crust have demonstrated the occurrence of successive melts and magmatic events, which are responsible for its compositional heterogeneities, and structure.

The thickness and the geotherm of the NPM lower crust are mainly constrained by interpretation of gravity anomalies and seismic tomography models. The depth of the Moho is estimated at ca. 30-40 km (Assumpção *et al.*, 2013; Chulick *et al.*, 2013; Van der Meijde *et al.*, 2013), while the high surface heat flow (ca. 65-135 mW/m²; Idárraga-García & Vargas, 2018; Christiansen *et al.*, 2022) and the thin lithosphere (<100 km; e.g. Afonso *et al.*, 2019) indicate the likelihood of high temperatures and a high geothermal gradient in the lower crust. However, another geophysical model, combining many types of data (tomography models, rock density, rock thermal conductivity and heat flow data), proposed a deeper Moho at 40-50 km, a crustal geotherm of 25°C/km for the first 30 km and a lithospheric thickness ranging between 115 and 200 km suggesting a colder thermal regime than previously proposed (Gómez-Dacal *et al.*, 2017, 2021). The petrological and geochemical nature and evolution of the NPM lower crust are still poorly characterised, (Pankhurst & Rapela, 1995), and its petrophysical characteristics remain unknown.

A detailed petrological, geochemical and microstructural characterisation of the NPM lower crust, will better constrain the magmatic and rheological relationships at the mantle-

crust transition. In this study, the rheology and the magmatic processes of the NPM lower crust has been investigated in detail by analysing the microstructure of granulites and websterites, as well as the chemical composition of minerals (major and trace elements). The combination of these new data allows us to present a model of the deformation, the thermal regime, the thickness, the origin and the evolution of the recent lower crust of the North Patagonian Massif. To build this model we use a collection of xenoliths of mafic granulites and websterites of Oligo-Miocene to Pleistocene volcanics from five different localities within the massif.

GEOLOGICAL SETTING

The North Patagonian Massif (NPM) is a plateau extended to 100 000 km², located in the provinces of Río Negro and Chubut, Argentina (39-43° S; Fig. 1). The NPM is bounded to the north by Neuquén and Colorado basins, and to the south by the Cañadón Asfalto and the San Jorge basins. To the East, it is underlain by Andean Cordillera mountain range and magmatic arc, resulting from the east-dipping long-lived ocean-continent subduction (e.g. Aragón *et al.*, 2011). The NPM, together with the Deseado massif to the south, is known to be one of the two massifs exposing basement rocks of the Patagonian geological province (Ramos, 2008). The basement outcrops show scarce Early to Late Paleozoic magmatic and metamorphic rocks (Cambro-Ordivician in the northeast, Devonian to Carboniferous in the west; Pankhurst *et al.*, 2006; Martínez Dopico *et al.*, 2011) and abundant Permo-Triassic magmatic rocks, the latter including granitoids, andesites and rhyolites (Pankhurst *et al.*, 2006). This exposed basement is overlain by Jurassic andesites, rhyolites and rare granitoids (Zaffarana *et al.*, 2020). Late Paleozoic to Jurassic magmatic rocks include Devonian to Permian I- to S- type magmatism (Oriolo *et al.* 2023) and the formation of the Choiyoi (Permian-Lower Trias; 295-248 Ma) and Chon Aike (Early Jurassic; 200-175 Ma) silicic large igneous provinces (SLIP;

Pankhurst & Rapela, 1995; Pankhurst *et al.*, 1998; Luppo *et al.*, 2018; Zaffarana *et al.*, 2020; Falco *et al.*, 2022; Gianni & Navarrete, 2022), and provide significant evidence for lower crustal growth and reworking of the NPM basement. In addition, mafic crustal xenoliths found in the Paso de Indios Paleogene basalts (Cañadón Asfalto Basin, south to the NPM) have been dated at 175.9 Ma by U-Pb zircon dating method (Castro *et al.*, 2011), and thus have been attributed to the formation of a residual crust during the Chon Aike SLIP. The lithosphere of the NPM is thought to have been thinned and reworked which is directly related to thermal erosion associated with the intense magmatic activity during both the Choiyoi and Chon Aike SLIP (Navarrete *et al.*, 2019; Gianni and Navarrete, 2022). This is supported by Re-Os systematics applied to peridotite xenoliths from Pleistocene volcanics which yielded Mesoproterozoic to Phanerozoic T_{RD} ages (1.3-0 Ga; Schilling *et al.*, 2008, 2017; Mundl *et al.*, 2016).

Finally, Cenozoic volcanic rocks, mainly Oligo-Miocene flood basalts (Cordenons *et al.*, 2020), form the upper part of the sequence. They belong to a Cenozoic intraplate large igneous province (LIP) with an asthenospheric mantle source that occurred in Patagonia (Kay *et al.*, 2007; Navarrete *et al.*, 2020) and are thought to include lower crust fractionation of the mantle source melts (Kay *et al.*, 2007; Cordenons *et al.*, 2020). The origin of the asthenospheric melting is not well constrained, in contrast to the magmatic evolution of the LIP (Kay *et al.*, 2007; Cordenons *et al.*, 2020). Early to middle Oligocene initial magmatic phases are mainly alkaline. Late Oligocene to Early Miocene phases are dominated by the production of tholeiitic flood basalts, followed by Middle to Late Miocene alkaline phases synonymous with the extinction of the LIP. The associated lower crust has not been characterised, however, extensive Cenozoic tectonics did not affect the NPM, except for

minor faulting and uplift when it affected all the surrounding basins (Aragón *et al.*, 2011). Therefore, the basement is compared to a cratonic block.

North Patagonian Massif xenoliths occur in Oligocene to Pleistocene volcanic rocks and display spinel and rare garnet peridotites, spinel pyroxenites, and granulites. Mantle peridotite xenoliths have been previously studied and discussed from petrological and geochemical perspectives (e.g. Bjerg *et al.*, 2005, 2009; Mundl *et al.*, 2016; Schilling *et al.*, 2017; Melchiorre *et al.*, 2020). However, despite their importance to characterise the lower crust, granulite xenoliths have not yet been studied in the NPM.

SAMPLE COLLECTION AND ANALYTICAL METHODS

Samples collection

Xenoliths were sampled within lava flows, basaltic necks or basaltic dykes from 5 different localities in northern Patagonia: Comallo, Cerro Traful, Cerro Aznares, Estancia Alvarez and Cerro Chenque (Fig. 1). The host rocks are Late Oligocene to Early Miocene alkaline trachybasalts and basalts with Cerro Chenque and Cerro Traful dated at 23 to 25 Ma and Cerro Aznares and Estancia Alvarez at 20 to 29 Ma (Mallmann, 2004; Bjerg *et al.*, 2005; Dantas, 2007; Mundl *et al.*, 2016; Melchiorre *et al.*, 2020), except Comallo where the host-lava flow was dated to the Early Pleistocene from 0.9 to 1.4 Ma (Mundl *et al.*, 2016). The xenoliths have an average diameter of 8 to 12 cm. A series of 20 mafic granulites and 3 websterites collected by T. Ntaflos and E. Bjerg in 2001, and a xenolith collection from C. Dantas (2007) consisting of 7 websterites and 1 mafic granulite from Cerro Aznares were used for this study (Table 1). Among these two collections, 9 granulites and 1 websterite were selected for major and trace elements bulk-rock analysis, 7 granulites and 2 websterites for

major element analysis on minerals, 5 granulites and 2 websterites for trace element analysis on minerals, 6 granulites and 2 websterites for detailed microstructural analyses.

Bulk-rock analyses

Bulk rock preparation has been done using the following protocol. All samples were crushed in an agate-crusher and subsequently reduced to powder using an agate disk mill. Bulk rock major and the trace elements Ba, Co, Cr, Ga, Ni, Rb, Sc, Sr, V, Zn and Zr were analysed with the sequential X-ray spectrometer Philips PW 2400, equipped with an Rh-excitation source (University of Vienna, Department of Lithospheric Research). Fused beads were produced at 950°C from a mixture of the specimen and $Li_2B_4O_7$ flux, diluted 1:5 to gain accurate and precise results. The trace elements were measured on powder pellets. Reference material used for the calibration were international geostandards BCR-1, BHVO-1, BIR-1, DR-N, SGD-1a, MO-1, GSR-2, GSR3-3 (Govindaraju, 1989). Replicate analyses of geo-standard GSR-3 gave an overall procedural uncertainty better than 2% for major elements and 5% (Cu=8.5%) for trace elements. The Loss On Ignition (LOI) has not been measured as the samples are fresh and there are no hydrous phases, which means the LOI is insignificant.

For small-size samples a bulk rock chemical analysis was not possible and their compositions have been calculated combining their mineral modal compositions obtained by Electron Backscatter Diffraction maps and mineral major elements composition obtained by microprobe analyses (Table 2). Bulk Fe_2O_3 was calculated based on the ratio Fe_2O_3/FeOt in two pyroxenes and spinel or titanomagnetite in two samples.

Backscatter images and minerals major elements compositions

Polished thick sections were covered with a 20 nm carbon deposit using a carbon evaporator Leica EM ACE600 for secondary Electron Microscope (SEM) observations and microprobe

measurements. SEM qualitative chemical analyses were carried out at the Géosciences Environnement Toulouse (GET) laboratory (CNRS-CNES-IRD-University Paul Sabatier, Toulouse), Observatoire Midi Pyrénées (Toulouse, France), using a Tescan Vega 4 equipped with an EDS Bruker Quantax 30mm². The analyses were conducted with an acceleration voltage of 20 kV, a probe current of 3 nA and a working distance of 15 mm.

Minerals major element analyses were carried out using a Cameca SX Five electron microprobe from the micro-characterisation centre Raimond Castaing (University Paul Sabatier, Toulouse). Measurements were made with an acceleration voltage of 15 kV and a probe current of 20 nA. Acquisition times were 10 s on peak and 5 s on either side of the peak for the continuous background. The reference materials used are natural or synthetic minerals as well as pure metals. The data summary and detection limits are available in Supplementary Table S1.

Clinopyroxene trace elements

Trace element contents in clinopyroxene was measured using the ELEMENT XR High Resolution ICP-MS (Thermo Scientific) coupled to the New Wave Research NWR213 Nd YAG 213 nm laser ablation unit from the GET laboratory (Observatoire Midi Pyrénées, Toulouse, France). Ablations were performed in a pure He atmosphere (500-600 xl/min) using a 50 or 30 μm spot size with a fluence of 1.5-2 J/cm^2, an energy of 20-30 % and 10 Hz repetition (pulse) rate. Counting time for one analysis was 210 s (60 s on gas blank to establish background, then 120 s for data acquisition followed by 30 s washout). The reference materials NIST SRM 610 and NIST SRM 612 were used as external reference material (Jochum *et al.*, 2011), bracketing at most 12 unknowns. CaO values (wt%) determined with the electron microprobe served as an internal reference material. The uncertainties for laser analysis range from 1 to 10% for most of the elements, and is at 15%

for Nb and Ta. The theoretical detection limits range from 10 to 60 ppb and for Sc and V is 100 ppb, for Ti is 2 ppm and for Ni and Cr is 0.7 ppm. Data reduction and processing were performed using the Glitter software (Van Achterbergh, 2001; Griffin *et al.*, 2008).

Thermobarometry

Modelling was performed in the Na_2O-CaO-K_2O-FeO-MgO-TiO_2-Al_2O_3-SiO_2-O_2 system, using the Perple_X 6.9.1 software and the internally consistent thermodynamic dataset (hp622ver) of Holland & Powell (2011). The solution models used were those of Fuhrman & Lindsley (1988) for plagioclase (Pl), Green *et al.* (2016) for clinopyroxene (Cpx) and melt, White *et al.* (2014) for orthopyroxene (Opx) and garnet (Grt), White *et al.* (2002) for spinel (Sp) and Holland & Powell (2004) for olivine (Ol). To avoid host lava interfering with xenolith bulk composition, calculated bulk rock compositions based on mineralogical proportions and microprobe analyses were preferred for pseudosection calculation. The O_2 content was calculated using the formula $O_{2\ mol} = 0.5*Fe_2O_{3\ mol}$. The TiO_2 from pyroxenes was not included in the bulk rock incrementation into Perple_X, as solution models of minerals without titanium were used. Four samples were selected for isochemical phase diagram calculations because they are well-preserved from lava interaction.

Crystallographic orientations of minerals

A mechanic-chemical polishing using a Vibromet (Buehler) was applied on 8 thick sections for 1h15 with a colloidal silica suspension (pH 10) to remove mechanically induced surface damage. Electron Backscatter Diffraction (EBSD) data acquisition was performed with a JEOL 7100 Secondary Electron microscope at the centre of micro-characterization Raimond Castaing (University Paul Sabatier, Toulouse), equipped with an EBSD camera CMOS Symmetry S2 (Oxford Instruments). Analyses were performed with an acceleration voltage of

20 kV, a probe current of 16 nA and a working distance of 15 or 17 mm with a stage tilt of 70°. Automatic indexing was performed using AZTec software (version 6.0 Oxford Instruments). The step size used for mapping varied between 15 and 20 μm depending on the grain size. The EBSD data were then processed in MATLAB (version R2020b) using the MTex toolbox (version 5.7.0; Bachmann *et al.,* 2010, 2011). A value of 10° as the cut-off angle for the determination of the grains was used, and low-angle boundaries are ≥ 2° and < 10°. Pole figures were plotted on a lower-hemisphere, equal-area stereographic projection. To avoid oversampling of large clinopyroxene and orthopyroxene crystals, pole figures were plotted with one point per grain, while plagioclase pole figures represent all the available measurements as twins increase the number of grains detected. The strength of the crystallographic preferred orientation was estimated using both the J- and M-indices (Bunge, 1982; Skemer *et al.*, 2005). In addition, the misorientation of each pixel was calculated relative to the mean orientation of its corresponding grain and then combined as maps of misorientation relative to mean grain orientation. In parallel, for each sample, pixel proportions relative to their misorientation angle were plotted in normalised histograms.

RESULTS

Sample description and petrography

Mafic granulites

Mafic granulite xenoliths are metagabbros and metagabbronorites composed of plagioclase (14-72 vol.%; Table 1), clinopyroxene (12-85 vol.%) ± orthopyroxene (0-52 vol.%), together with either spinel (samples CXTRA1, CXTRA4, CXALV1, CXCHE4 and CXAZN2; Fig. 2a), titanomagnetite (samples CXAZN1, CXCHE3 and CXTRA2; Fig. 2b, c) or without oxide in sample CXCHE2 from Cerro Chenque (Fig. 2f). Sample CXALV1 from Estancia Alvarez is characterised by two types of spinel, Ferrian-pleonaste and Al-magnetite, which can form a

symplectite with a single-crystal-like shape (Fig. 2d). Accessory olivine was found only in the sample CXAZN1 (Fig. 2c). Traces of ilmenite also occur in this sample.

Mafic granulites display a granoblastic texture with clinopyroxene- or plagioclase-rich layers where crystals are flattened and slightly elongated (aspect ratio up to 2:1; Fig. 2b, c, e). The grain size distribution is rather unimodal with clinopyroxene, plagioclase and orthopyroxene ranging from 0.3 to 5 mm (Fig. 2). Many samples display linear grain boundaries (samples CXALV1, CXAZN2, CXCHE3, CXTRA1, CXTRA4) with numerous 120° triple junctions (Fig. 2a, b, e) and some samples present slightly curved grain boundaries (CXAZN1, CXCHE4; Fig. 2c). Metagabbro CXCHE2 has a texture that differs from the suite by exhibiting fine (ca. 0.3 mm) to very coarse plagioclase grains (up to 1 cm) together with curved grain boundaries and rare 120° triple junctions (Fig. 2f). Albite twinning is observed in all samples and is sometimes tapered (Fig. 2a). Partial melting during xenolith transport by the host lava produces, at the expense of orthopyroxene, subhedral olivine II grains that can reach 100 μm in size, orthopyroxene II rims (<50 μm) on orthopyroxene I grains and interstitial glass and potassic feldspar (Supplementary Fig. S1). These reactions are almost absent (e.g. CXTRA4) to ubiquitous and sometimes form pockets (e.g. CXCHE3; Fig. 2b). Spongy rims of clinopyroxene II can also be observed on clinopyroxenes, produced during host lava transport, usually a few micrometres in size, except in sample CXAZN1 where they are 50 μm width (Fig. 2c). Finally, clinopyroxene in some samples displays Fe-Ti exsolution lamellae too thin to be analysed with the microprobe.

Websterites

Spinel-websterites from Comallo, Cerro Aznares and Cerro Chenque (samples CO10A1, PM6C8 and CXCHE1) display a granoblastic texture. They are composed of clinopyroxene and orthopyroxene with a grain size varying from 0.5 to 3 mm, spinel (grain size from 0.1 to

1.5 mm), and a small amount of plagioclase (0.1-1 mm; Fig. 2g; Table 1). No shape preferred orientation is observed, and almost no deformation markers are observed, as there is no undulose extinction, grain boundaries between phases are slightly curved, and 120° triple junctions are common.

Reactions with the host lava, similar to those in granulites, result in the crystallisation of secondary olivine, clinopyroxene, K-feldspar, as well as the formation of glass.

Bulk rock chemistry

Major elements

All xenoliths have a SiO_2 contents ranging from 44 to 53 wt% while Mg# (100 x Mg/(Mg+Fet), mol) varies from 53 to 79 (Fig. 3; Table 2). The Mg# is high in websterites (samples CO10A1, CXCHE1 and PM6C8), in three metagabbronorites (CXTRA1, CXTRA4 and CXAZN2) and in a metagabbro (CXCHE2). These samples plot in the mafic 1 field from Kempton & Harmon (1992; Fig. 3). Three samples plot in the primitive basalt fields (CXTRA2, CXCHE2 and CXAZN1). The SiO_2/Al_2O_3 ratio varies from 2.16 to 3.95, with the highest ratio found in the websterite from Comallo and the lowest in the metagabbro from Estancia Alvarez. Some samples have lower SiO_2/Al_2O_3 ratios (CXTRA4, CXALV1, CXAZN2, CXCHE4) that can be attributed to the accumulation of Al-rich mineral phases such as plagioclase or spinel (Fig. 3). The Na_2O content covers a wide range from 0.54 to 3.88 wt% (Table 2). The Al_2O_3, Na_2O, Sr and Ba contents correlate positively with the volume proportion of plagioclase and negatively with the MgO, Ni, Co and Cr contents.

The bulk rock compositions of the investigated xenoliths plot within the mafic 2, mafic 3 or intermediate fields of the granulite classification proposed by Kempton & Harmon (1992; Fig. 3). When plotted within this classification, the North Patagonian Cenozoic lavas (Kay *et al.*, 2004, 2007; Jacques *et al.*, 2014; Massaferro *et al.*, 2014, Asiain *et al.*, 2022) form

a field that follows the alkaline differentiation trend, characterised by a decrease in Mg# with a constant SiO_2/Al_2O_3 ratio (Fig. 3). Titanomagnetite-bearing granulites have higher abundances of TiO_2 (0.73-1.38 wt%) than other granulites (0.19-0.57 wt%). Granulite xenoliths from Pankhurst & Rapela (1995; Sierra de los Chacays, southern NPM) and Castro *et al.* (2011; Pasos de Indios, Cañadon Asfalto basin) display similar Mg# and SiO_2/Al_2O_3 ratios for most of them and plot in the mafic 1, 2 or 3 fields (Fig. 3).

Trace elements

The xenolith suite, excluding CXTRA2, displays homogeneous and low concentrations of incompatible elements such as Nb, Zr, Y and Rb, with Nb ranging from 2 to 8 ppm, Zr from 8 to 46 ppm, Y from 3 to 17 ppm and Rb from 7 to 15 ppm (Table 2). The factor of variation ranges between 2 and 6 across samples. In contrast, sample CXTRA2 displays high concentrations of Nb (29 ppm), Zr (141 ppm), and Rb (37 ppm). Some compatible elements, such as Ni (between 24 and 242 ppm) and Co (between 29 and 75 ppm), show heterogeneous concentrations within the suite (Table 2). Sr and Cr display higher abundances compared to the above elements (334-1291 ppm and 52-450 ppm respectively), while Ba, which is compatible with plagioclase, has highly variable concentrations ranging from 2 to 695 ppm, representing a 400-fold variation.

Titanomagnetite-bearing granulites show higher abundances of Y (9-17 ppm) than other granulites (3-7 ppm), a trend that is also observed for TiO_2. The whole xenolith suite

displays a continuous major and trace element compositional range, with no compositional gap between metagabbro, metagrabbronorite, and websterites.

Minerals major elements composition

Clinopyroxene

Clinopyroxene is mainly Al-diopside (Al_2O_3 > 4 wt%), although diopside sensu stricto occurs in the titanomagnetite and olivine-bearing metagabbronorite CXAZN1 from Cerro Aznares, and Al-Augite in sample CXCHE2 and some websterites of the suite from Dantas (2007; PM6Cx from Cerro Aznares; Fig. 4a, c; Supplementary Table S1). The clinopyroxene crystals of all the investigated samples have an Al distribution between IV and VI sites that follows a ratio close to 1:1 (Fig. 4b), and they fall within the granulite field of the classification of Aoki & Kushiro (1968; Fig. 4b). The Al_2O_3 content varies between 5.7 and 9.4 wt%, but for the metagabbronorites CXAZN1 and the websterite suite PM6Cx, values range from 2.5 to 4 wt% and from 3.1 to 4.1 wt%, respectively (Fig. 4c). Mg# ranges from 66 to 79, except for the websterites PM6C8 and the websterite suite PM6Cx from Cerro Aznares which have high Mg# values (83-90). The investigated suite is characterised by a negative correlation between Al_2O_3 content and Mg#, except for sample CXAZN1 (Fig. 4c). Samples from Cerro Aznares (CXAZN1, CXAZN2, PM6C8, suite PM6Cx) have low TiO_2 content (0.25-0.48 wt%) while those from Comallo, Cerro Traful and Estancia Alvarez display a higher TiO_2 content (0.6-1.12 wt%) (Fig. 4d). Finally, the Cerro Chenque xenoliths have high TiO_2 content (0.84-1.72 wt%). The calculated Fe_2O_3 content (by stoichiometry) is homogeneous between samples (1.5-3.5 wt%), whereas FeO content may vary between samples (7.7-8.3 wt% in samples CXCHE2 and CXAZN1 respectively and 3.5-5.8 wt% for the others; Supplementary Table S1). The Na_2O content is always less than 1 wt%. The compositions of the clinopyroxene spongy rims are similar to those of the cores, except for the TiO_2 contents which can decrease

362 by <0.2 wt%. Clinopyroxene II and spongy clinopyroxene rims (Supplementary Fig. S1)
363 measured in samples CXAZN1, CXCHE2 and CXCHE3 has Al_2O_3 contents lower than 1
364 wt% and has Mg# values bracketed between 75 and 79. Otherwise, it has similar
365 compositions to clinopyroxene I.
366
367 *Orthopyroxene*
368 Orthopyroxene from metagabbros and metagabbronorite is Al-enstatite (Al_2O_3 content
369 between 4 and 6.5 wt%) and displays a Mg# varying from 71 to 77 (Fig. 5a, c; Supplementary
370 Table S1). The Mg# and Al_2O_3 diagram displays a negative correlation trend as already
371 observed for clinopyroxene (Fig. 4). As for clinopyroxene, the orthopyroxene from sample
372 CXAZN1 (Cerro Aznares) has significantly lower Mg# (61-62), and Al_2O_3 content (2 wt%)
373 than other granulites (Fig. 5b). Orthopyroxene from websterites CO10A1 (Comallo) and
374 PM6C8 (Cerro Aznares) has slightly higher Mg# (77-81) and similar Al_2O_3 content (4.9-5.4
375 wt%) than other granulites. Cerro Aznares websterites from Dantas (2007; suite PM6Cx) have
376 high Mg# (80-86) and Cr_2O_3 content (up to 0.37) but display low Al_2O_3 content (1.2-3.2
377 wt%), similar to those from CXAZN1. Orthopyroxene II measured in samples CXTRA4,
378 CXAZN1, CXAZN2, and CXCHE2 has the same composition as orthopyroxene I.
379
380 *Plagioclase*
381 Plagioclase varies from bytownite to andesine (An_{88-40}) with orthoclase contents always <5
382 mol% (Fig. 5d; Supplementary Table S1). Plagioclase from metagabbronorite granulites
383 CXAZN2, CXTRA1 and CXTRA4 is the most calcic plagioclase of the whole suite with a
384 bytownite (An_{88-65}) composition. Websterites CO10A1 and PM6C8 have accessory
385 plagioclase that varies between bytownite and labradorite (An_{66} and An_{63-72}, respectively).

386 The plagioclase from CXALV1 and CXCHE3 is essentially labradorite (An_{65-46}), whereas that
387 of the samples CXCHE2 and CXAZN1 is essentially andesine (An_{50-40}).
388
389 *Spinel group*
390 In spinel-websterites and granulites, spinel is usually pleonaste (samples CXTRA1, CXTRA4,
391 CXAZN2, CO10A1, PM6C8; Supplementary Table S1; Supplementary Fig. S2). TiO_2 and
392 Cr_2O_3 contents are low (<0.56 wt% and <1.61 wt%, respectively) and Fe_2O_3 content increases
393 up to 13 wt% when the Al_2O_3 content decreases from 62 to 52 wt% (Supplementary Table
394 S1). Websterite PM6C8 is characterised by a spinel with a higher Mg# (67-69) compared to
395 other samples (56-61). Metagabbro CXALV1 (Estancia Alvarez) hosts two different types of
396 spinel: ferrian-pleonaste and Al-magnetite (Supplementary Fig. S1). They have low Cr_2O_3
397 <0.2 wt% and MnO and 0.17-0.32 wt% contents. Ferrian-pleonaste has a Mg# of 41-47, an
398 Al_2O_3 content of 41-43 wt%, a high Fe_2O_3 (20-23 wt%) and a low TiO_2 (1.5-2 wt%). Al-
399 magnetite has a lower Mg# (20-24), lower content of Al_2O_3 (15-19 wt%), higher Fe_2O_3 (36-39
400 wt%) and TiO_2 (6-8 wt%) than other spinels.
401 Titanomagnetite in samples CXAZN1 and CXCHE3 is characterised by low contents
402 of MgO (2.1-3.6 wt%) and Al_2O_3 (2.1-5.1 wt%). Titanomagnetite in sample CXCHE3 has

403 TiO_2 contents of 13.7-15.1 wt% and FeO_t contents of 68.3-73.2 wt%. CXAZN1 has higher
404 TiO_2 contents (21.6-22.6 wt%) but lower FeO_t contents (65.7-67.6 wt%).
405
406 *Accessory minerals (olivine, ilmenite)*
407 Metaggabronorite CXAZN1 displays accessory olivine with a Mg# of 61 and traces of
408 ilmenite (Supplementary Table S1).
409
410 **Clinopyroxene trace elements**
411 *Rare Earth Elements*
412 All the investigated samples are characterised by smooth convex chondrite-normalised rare
413 earth elements (REE) patterns associated with an enrichment in medium rare earth elements
414 (MREE; Sm to Ho) over light rare earth elements (LREE; La to Nd) and heavy rare earth
415 elements (HREE; Er to Lu; $0.1<La_n/Sm_n<0.9$; $0.3<Yb_n/Sm_n<0.4$; Fig. 6a; Table 3). The
416 metagabbronorites from Cerro Aznares display a higher REE concentration than the other
417 samples, especially metagabbronorites CXAZN1 and PM6C10, the former displaying a
418 negative Eu anomaly and HREE enrichment. The two metagabbros (CXALV1 and CXCHE2)
419 have similar MREE and HREE concentrations but sample CXALV1 has lower LREE
420 contents that widely vary between clinopyroxene grains (see Supplementary Fig. S3), and a
421 slight positive Eu anomaly. Websterite CO10A1 from Comallo displays a similar pattern to
422 that of websterite PM6C8 but at a higher level of concentration (Fig. 6a). Websterite suite
423 PM6Cx from Dantas (2007) displays similar patterns and REE concentrations bracketed

between the two investigated websterites CO10A1 and PM6C8, except for LREE values which can reach lower concentrations than in websterite PM6C8.

Trace Elements

The investigated clinopyroxene grains are characterised by a Ti anomaly that can be strongly negative (sample CXAZN1), slightly negative (samples CO10A1, CXTRA4, CXALV1, PM6C8, PM6C10), or slightly positive (sample CXCHE2; Fig. 6b). All samples display a Zr-Hf negative anomaly, deeper in sample CXALV1. With the exception of sample CXALV1, all the investigated granulites have a negative Sr anomaly, which is even stronger for the two metagabbronorites CXAZN1 and PM6C10 (Fig. 6). Clinopyroxene from the two websterites display a positive Sr anomaly, deep in sample PM6C8 and weak in sample CO10A1.

Thermobarometry

The Fe-Mg exchange two-pyroxene thermometer from Wells (1977) was applied to all the investigated samples that contain both pyroxenes (4 metagabbronorites, 2 metagabbros, 2 websterites; Table 1) and on the websterite suite PM6Cx from Dantas (2007). It yields a temperature range of 762-1070°C ±70°C and mafic granulites and websterites have similar temperature ranges.

Pseudosection calculations were applied to two metagabbronorites (CXTRA1, CXTRA4) and two websterites (CO10A1, PM6C8). Among these samples, sample CXTRA4 from Cerro Traful is representative of the main rock type, i.e. metagrabbronorite with modal proportions of plagioclase > clinopyroxene > orthopyroxene > spinel (Table 1), so results from this sample are presented in detail (Fig. 7a). Pseudosection calculations applied to other samples are presented in Supplementary Fig. S4. The metagabbronorite CXTRA4 contains 55 vol.% plagioclase, 31 vol.% clinopyroxene, 11 vol.% orthopyroxene, spinel as an accessory

449 mineral and 2 vol.% interstitial olivine (olivine II) which is not part of the main paragenesis
450 (Table 1). The comparison of pseudosection topology and petrological observations, as well
451 as the comparison between calculated and observed modal proportions, define P-T conditions
452 at 9-9.8 kbar and 1000-1050°C (red area in Fig. 7a). In Figure 7b, all pseudosection
453 calculations are reported and yield pressure conditions between 7 and 11.8 kbar and
454 temperature between 760 and 1150°C within the orthopyroxene-granulite stability field (Fig.
455 7b; Supplementary Fig. S4). This estimation includes both the Pleistocene xenolith (sample
456 CO10A1, 7-8.8 kbar, 770-930 °C; Fig. 7b) and the Oligo-Miocene xenoliths (all the other
457 samples). In conclusion, the pseudosection calculations with petrological observations allow
458 to define a geotherm between 28°C/km and 31.5°C/km (Fig. 7b).
459
460 **Microstructures**
461 *Crystallographic Preferential Orientation (CPO)*
462 *Clinopyroxene.* Most of the mafic granulite samples (i.e. metagabbros and
463 metagabbronorites) from all localities display weak CPO patterns (J-index 1.49-2.8; M-index
464 0.007-0.036) with a point concentration on [100] axes parallel to X that could represent a
465 lineation, and a more scattered distribution on [010] and [001] axes (Fig. 8). The metagabbro
466 from Cerro Traful, CXTRA1, display strong clusters on [010] axes parallel to Z,
467 perpendicular to the layering and [001] axes forming a weak girdle in the XY plane with
468 concentration points within the layering. [100] axes in that sample weakly cluster near [001]
469 axes concentration points. The metagabbronorite CXCHE4 displays a second point
470 concentration on [100] near Z, and [010] axes cluster parallel to Y. The titanomagnetite-
471 metagabbronorite sample CXAZN1 from Cerro Aznares displays a CPO similar to sample
472 CXTRA1 from Cerro Traful, with a point concentration of [010] axes parallel to Z and [001]
473 axes that girdle within the XY plane forming the layering. [100] axes display a point

concentration at 40° to X (Fig. 8). Websterite samples CO10A1 and PM6C8 show maximum clustering of [001] axes sub-parallel to X, [010] axes are perpendicular to the layering and [100] axes display random orientations.

Orthopyroxene. Mafic granulites and websterites have weak orthopyroxene CPO patterns (J-index 1.50-2.18; M-index 0.015-0.025, Fig. 8), as for clinopyroxene. Sample CXTRA1, CXCHE4 and CXAZN1 [001] axes form a point concentration parallel to X, and a possible girdle in the XY plane (well present in sample CXTRA1), and [010] axes display a weak point concentration parallel to Z (Fig. 8). The spinel-metagrabbronorite CXTRA4 displays a point concentration of [100] axes sub-parallel to X, and few orthopyroxene grains from samples CXALV1 display similar orientations (Fig. 8). Websterite PM6C8 displays [001] axes sub-parallel to X, and parallel to clinopyroxene [001] axes. CO10A1 doesn't have a readable CPO as the number of indexed grains is too low.

Plagioclase. Mafic granulites display weak CPO patterns, as indicated by the J-index (2.26-4.31) and M-index (0.017-0.038), except for the sample CXAZN1 (M-index 0.067; Fig. 9a). Most of the mafic granulites display [010] plagioclase axes parallel or at a low angle to Z, [100] axes within the XY plane, and scattered [001] orientations. In sample CXAZN1, [100] axes display a weak point concentration parallel to X. Sample CXTRA1 has a maximum [001] point concentration parallel to Z (Fig. 9a). Websterite PM6C8 displays [001] axes at low angle to X and to the pyroxenes [001] orientations. [100] axes cluster parallel to Z, as [010] axes weakly cluster near Y. J-index and M-index are extremely high (10.10) but it may

494 be related to the low proportion of indexed plagioclase in this sample (495 grains and <1.6
495 vol%; Fig. 9).
496
497 *Intragranular deformation*
498 *Clinopyroxene.* Intragranular deformation (i.e. misorientations within grains) in
499 clinopyroxene is well developed in metagabbronorites CXCHE4, CXCHE2, CXTRA1 and
500 CXTRA4, with respect to the whole suite (Fig. 10a). In these samples, the distribution of
501 deformation affects all grain sizes, with subgrain boundaries that are more or less well
502 defined, even if it is more heterogeneous within the sample CXCHE2 where intragranular
503 deformation spares some grains and deeply penetrates the others. Clinopyroxene from the
504 metagabbro CXALV1, like that observed in sample CXCHE2, displays grains with and
505 without subgrains, for similar grain size (Fig. 10a). However, in sample CXALV1
506 clinopyroxene grains with many misorientations can have polygonal grain boundaries while
507 undeformed grains display linear grain boundaries and appear to penetrate deformed grains. In
508 these samples, clinopyroxene subgrain boundaries are either perpendicular to the long axes of
509 the grains or form a cone shape with a high degree of misorientation at the tip of the grains
510 (Fig. 10a).
511 The distribution of the misorientation axes within the grains indicates that more than
512 half of misorientations are bracketed between > 1 and 3° for both clinopyroxene and
513 orthopyroxene (Fig. 10c). Among the studied samples, the websterites (PM6C8 and CO10A1)
514 display weak internal deformation (29 and 18 % of the clinopyroxene area, respectively) and
515 rare subgrain boundaries (Fig. 10a, c).
516 Clinopyroxene misorientation axes at low angle boundaries or subgrain boundaries are
517 distributed around both [001] and [010] axes in the samples CXTRA1, CXTRA4, CXALV1,

CXCHE4 and PM6C8, and only around [010] axis in CXCHE2 and CXAZN1 samples (Fig. 9b, c).

Orthopyroxene. Samples CXTRA1, CXTRA4, CXCHE2 and CXCHE4, display the stronger orthopyroxene intragranular deformation (58-72 % of the orthopyroxene area; Fig. 10b, c) with this deformation occurring uniformly throughout the samples. Subgrain boundaries are more often perpendicular to the long axes of the grains than in clinopyroxenes, even if cone-shaped subgrain boundaries are also present at the grain tips. In other metagabbros, metagabbronorites and websterites, orthopyroxene grains display weak internal deformation (7-33 % of the orthopyroxene area; Fig. 10b, c) and are mostly composed of subgrain with low misorientation angles (< 3°) compared to the deformed sample group (Fig. 10c).

Misorientation axes at subgrain boundaries of all samples are preferentially arranged around the [010] axis, except CO10A1 which shows an arrangement around the [100] axis (Fig. 9b). However, this result must be taken with caution as the subgrain boundaries dataset for this sample is small.

Plagioclase. In samples CXTRA1, CXTRA4, CXCHE2 and CXCHE4, a large area of the plagioclase is affected by intragranular deformation (at least 84% with misorientation > 1°), similar to the observed deformation in the associated pyroxenes (Figs. 11a and 10). Plagioclase subgrain boundaries are more often angular to the grain tips than perpendicular to the long axis of the grains. In sample CXCHE2, plagioclase displays many long (up to 2 mm) and non-linear grain-cross-cutting subgrain boundaries. In sample CXAZN1, the intragranular deformation is homogeneous and affects a larger area in plagioclase (62% with misorientation > 1°) than in pyroxene, where it reaches 31% for clinopyroxene and 10% for orthopyroxene, respectively (Figs. 10a, c, 11). Sample CXALV1 displays less intragranular deformation (17% of the plagioclase area) than other mafic granulites (62-89% of the plagioclase area; Fig. 11a,

543 b). It also shows a bimodal distribution between large plagioclase grains with subgrains, and
544 smaller grains without subgrains. Large grains have curved grain boundaries and are
545 surrounded by numerous small undeformed grains with linear boundaries. Albite twinning
546 occurs in both large deformed grains and small undeformed grains (Fig. 11a).
547 Misorientation axes at subgrain boundaries cluster around the [100] axis and less
548 frequently around the $[20\bar{1}]$ axis in the spinel granulites CXTRA1, CXTRA4 and CXCHE4
549 (Fig. 9b). In the other samples, they cluster around the $[30\bar{1}]$ axis.
550

551 **DISCUSSION**

552 **Protoliths of mafic granulite and websterite xenoliths**

553 The mafic granulites, except the samples CXTRA2 and CXCHE2, display a well-defined
554 pyroxene and plagioclase (or spinel)-rich layering (Fig. 2). The presence of this layering is in
555 agreement with a magmatic protolith. The studied samples plot within the Mafic 1 (Mg# >
556 0.7; Fig. 3), Mafic 2 (Mg# = 0.6 to 0.7) or Mafic 3 (Mg# <0.6) field defined by Kempton &
557 Harmon (1992). They suggested that the Mafic 1 field could correspond to granulites from
558 cumulates *sensu stricto* from basaltic melts or to basaltic melts that have accumulated mafic
559 phases. The authors also suggested that the Mafic 2 field could correspond to i) granulites
560 from cumulates *sensu stricto* derived from evolved melts (Mg# of 0.4 to 0.5), in contrast to
561 the melts that sourced the Mafic 1 group granulites, although this is unlikely because they
562 generally have high incompatible trace element contents, or to ii) solidified evolved melts that
563 have accumulated a large proportion of phenocrysts. In addition, they proposed that the Mafic
564 3 field does not correspond to cumulates because they display a low SiO_2/Al_2O_3 ratio
565 compared to basalts and their differentiates (Fig. 3). Therefore, they are either solidified
566 intermediate melts formed after fractional crystallisation, where feldspar dominates the
567 assemblage, or residues from metasediments or intermediate igneous rocks after partial

568 melting. Furthermore, the calculated pressures and temperatures are homogeneous between
569 the investigated samples (Table 1; Fig. 7b), despite variations in the mineralogy and the bulk
570 rock and mineral compositions (e.g. plagioclase variation from bytownite to andesine;
571 Supplementary Table S1; Fig. 5d). The positive correlation between plagioclase Na_2O content
572 and bulk rock Na_2O composition suggests that plagioclase composition is primarily controlled
573 by the bulk rock Na_2O budget (Supplementary Table S1). This suggests that these multiple
574 variations (mineralogical and chemical) are not only controlled by pressure and temperature
575 conditions but also reflect the composition and evolution of the parent magma.
576 The cpx upward convex REE chondrite normalised patterns of mafic granulites and
577 websterites are similar to those of cpx phenocrysts (Beccaluva *et al.*, 2009; McCoy-West *et*
578 *al.*, 2010; Desta *et al.*, 2014; Natali *et al.*, 2016; Lee *et al.*, 2021) or megacrysts (Sun *et al.*,
579 2022) from LIP basalts (Fig. 6; and see comparison in Supplementary Fig. S5). Websterite
580 xenoliths from Cerro Aznares studied by Dantas (2007; suite PM6Cx) display similar patterns
581 and are interpreted as cumulates crystallised from a basalt (Fig. 6). Furthermore, LIP basalts
582 are typically formed from mantle sources without crustal mixing or contamination (e.g. Bryan
583 & Ferrari, 2013). This suggests that a fraction of a basaltic liquid in a LIP context may have
584 been stored in the crust and formed granulite protoliths and that the residue of the fraction
585 may have formed surface basalt without contamination. Kay *et al.* (2007) proposed that the
586 tholeiitic magmatic phase of the Cenozoic (Oligo-Miocene) basaltic LIP in the North
587 Patagonian region (the Somuncura LIP) produced slightly differentiated volcanic products
588 associated with magmatic underplating processes at the crust-mantle boundary and minor
589 crustal contamination. Both mantle and crustal sources have been proposed for the Permo-
590 Trias and the Jurassic SLIP (Pankhurst *et al.*, 2006; Kay *et al.*, 2007; Zaffarana *et al*., 2020).
591 Pankhurst *et al.* (1998) even suggest that primary basalts are rare throughout the Jurassic
592 Chon Aike province and that most mantle-derived magmas have undergone a mixing process

593 with crustal-derived magmas. Volcanic rocks produced during the two Choiyoi and Chon
594 Aike SLIP - mainly dacites and rhyolites and andesites, respectively - are more differentiated
595 than the investigated xenoliths suite. However, it is recognised that SLIP also produced mafic
596 cumulates within the lower crust and crust-mantle boundary (e.g. Bryan & Ferrari, 2013). In
597 order to assess the affinity between the investigated xenoliths and the LIP-related basalts from
598 the region, the REE composition of melts in equilibrium with the cpx was calculated, using
599 partition coefficients between the cpx and a tholeiitic basalt from Fujimaki *et al.* (1984; Fig.
600 12). We assume that clinopyroxene REE composition did not change between magmatic
601 protolith formation and metamorphism stage. The calculated melt REE patterns were
602 compared with REE patterns from Oligo-Miocene and Quaternary basalts (Stern *et al.*, 1990;
603 Kay *et al.*, 2004, 2007; Jacques *et al.*, 2014; Massaferro *et al.*, 2014; Asiain *et al.*, 2022). In
604 Figure 12, the calculated REE patterns are generally consistent with those of the Cenozoic and
605 Quaternary basalts, especially the samples CO10A1, CXTRA4, CXCHE2, and MREE and
606 HREE of CXALV1. Nevertheless, there is no data on basaltic rocks from Jurassic (mainly
607 andesites; López De Luchi & Rapalini, 2002; Zaffarana *et al.*, 2019, 2020) or Permo-Trias
608 SLIPs (mainly dacites or rhyolites; Martínez Dopico *et al.*, 2019). Therefore, these results
609 suggest that the studied suite of metagabbro, metagabbronorite and websterite was initially
610 formed by basaltic cumulates, but we cannot conclude which LIP, rather Permo-Triassic,
611 Jurassic or Cenozoic, contributed to the formation of these samples and the crustal growth of
612 the NPM (Fig. 13).
613

614 **Magmatic and deformation processes recorded by the xenolith suite**

615 *Mafic Granulites*

616 The metagabbro CXCHE2 from Cerro Chenque displays very coarse grains (porphyritic-like
617 texture) and augite twinning known to be a magmatic feature (Griffin *et al.*, 2022; Fig. 10a).

618 The clinopyroxene CPO in this sample is weak, lacking clear concentration axes and
619 dominant slip systems (Fig. 8), suggesting the preservation of a magmatic texture.
620 Nevertheless, at crystallographic scale, some large grains display intense dislocation creep,
621 expressed by numerous subgrain boundaries (subgrains with misorientations > 4° and < 10° in
622 Figs. 10, 11), and well-concentrated misorientation axes along [010] axes, indicating the
623 activation of the (100)[001] slip system (Fig. 9; Griffin *et al.* 2022). Dislocation creep
624 mechanisms are associated with curved grain boundaries known to be related with high-
625 temperature recrystallisation mechanisms (Passchier & Trouw, 2005). Sample CXCHE2 has
626 preserved microstructural evidence of its magmatic protolith although this texture has been
627 partially overprinted by high-temperature deformation. While the other xenoliths display more
628 120° triple junctions than sample CXCHE2 and none of the above magmatic features (Fig. 2),
629 sample CXCHE2 could represents the protolith that formed more recently than the other
630 samples before their ascent as xenoliths.

631 All other mafic granulites are characterised by the presence of intragranular
632 misorientation and subgrain boundaries in pyroxenes and plagioclase, as well as conical albite
633 twins. These features are indicative of plastic deformation by dislocation creep (Figs. 10, 11).
634 However, the intensity of deformation varies between the mafic granulite samples. The most
635 deformed rocks include CXTRA1, CXTRA4 from Cerro Traful, CXCHE4 and CXCHE2 (the
636 latter discussed above) from Cerro Chenque (Figs. 10, 11). These two localities represent the
637 northern and southern ends of the study area, suggesting only weak deformation throughout
638 the region (Fig. 1). Sample CXAZN1 from Cerro Aznares displays less intragranular
639 deformation, particularly in orthopyroxene (Figs. 10c, 11).

640 The entire mafic granulite suite is characterised by relatively weak clinopyroxene CPO
641 patterns (J-index up to 2.4; Figs. 8, 9), even in samples displaying important intragranular
642 deformation (CXTRA1, CXTRA4, CXCHE2, CXCHE4; Fig. 10). In samples CXTRA1 and

643 CXAZN1, the clinopyroxene CPO patterns show a concentration of [001] axes parallel to X
644 and [010] axes parallel to Z, indicating the possible activation of the (010)[001] slip system
645 (Fig. 8). While this system is known, and it has been observed in the lower crust (van der
646 Werf *et al.*, 2017) it is less common in clinopyroxene (SL-type, Helmstaedt *et al.*, 1972,
647 Zhang *et al.*, 2006; van der Werf *et al.*, 2017) because it is difficult to activate (Amiguet,
648 2009). In samples CXTRA4 and CXCHE4, the clinopyroxene [100] axes are parallel to X,
649 and two other axes are more scattered. The alignment of clinopyroxene [100] axes parallel to
650 X is quite unusual, but the [100](001) slip system is described and is considered to play a
651 minor role in clinopyroxene strain accommodation (Amiguet, 2009). In the deformed samples
652 CXTRA1, CXTRA4 and CXAZN1, the orientation of orthopyroxene axes is similar to
653 clinopyroxene axes (Fig. 8), suggesting similar formation or deformation conditions. The
654 alignment of both clinopyroxene and orthopyroxene [100] axes parallel to the lineation is
655 uncommon in terrestrial rocks. However, in the subcontinental mantle, Kourim *et al.* (2015)
656 report a weak alignment of both clinopyroxene and orthopyroxene [100] axes with the
657 lineation and weak CPO, suggesting a post-deformation recrystallisation event. Furthermore,
658 a concentration of clinopyroxene [100] axes representing the lineation has been observed in
659 clinopyroxene-rich meteorites and interpreted as a cumulate texture (e.g. Daly *et al.*, 2019).
660 These results suggest that the clinopyroxene and orthopyroxene CPO with [100] axes parallel
661 to X could represent primary magmatic crystallisation and early weak deformation.
662 In these four samples (CXTRA1, CXTRA4, CHCHE4, CXAZN1), plagioclase
663 displays internal deformation (Fig. 11), and similar to pyroxenes, the CPO is weak. The
664 plagioclase CPO consistently displays a concentration of [010] axes pattern parallel to Z and a
665 concentration point of [100] axes within the foliation plane (Fig. 9). The presence of
666 plagioclase [100] axes parallel to the lineation is a common observation. When plagioclase
667 and clinopyroxene are deformed coherently, plagioclase [100] axis is parallel to

clinopyroxene [001] axis. Therefore, the slight angle difference between the plagioclase [100] axis and the pyroxenes [100] or [001] axes suggests a change in constraint direction. The fabric associated with magma crystallisation could be represented by a [100](010) fabric in plagioclase and either a [001](010) or [100](001) fabric in pyroxenes, with both clinopyroxene and orthopyroxene developing the same fabric within a sample.

The deformed samples display intragranular deformation, sub-grain boundaries and slightly curved grain boundaries (Figs. 2, 10, 11) suggesting plastic deformation. To assess the plastic deformation recorded by minerals through dislocation creep and identify the slip system, misorientation axes serve as useful indicators (Fig. 9). Samples with significant internal deformation show clinopyroxene low-angle misorientation axes aligned with either the [010] and [001] axes or the [010] axis (Fig. 9). Although these paired axis rotations have been associated with mechanical twinning (Frets *et al.*, 2012; Soret *et al.*, 2019; Taufner *et al.*, 2021), which was not observed in the suite, Griffin *et al.* (2022) correlate such low-angle misorientations with the activation of paired dominant [001](100) and minor [100](001) slip systems. They argue that this combination is common in "most Earth-relevant extrinsic conditions". Thus, the presence of [010] misorientations may indicate activation of the clinopyroxene [001](100) slip system which has been described as the dominant slip system at 800-1000°C (Raterron *et al.*, 1994; Amiguet, 2009; Wang *et al.*, 2012). These interpretations suggest that plastic deformation in clinopyroxene in our samples is supported by the [001](100) slip system and confirm that clinopyroxene CPO with [100] parallel to X (Fig. 8) represents a magmatic event. Orthopyroxene displays [010] low-angle misorientation in all samples, which correlates with the activation of the [001](100) slip system, which is by far the most commonly activated to accommodate deformation (e.g. Wang *et al.*, 2012; Bernard *et al.*, 2021). Moreover, plagioclase low-angle misorientation axes align with the [100] axis,

692 which is attributed to the [001](010) slip system (van der Werf *et al.*, 2017; Allard *et al.*,
693 2021).

694 In summary, the slip systems suggested by the low-angle misorientation analysis were
695 systematically [001](100) in clinopyroxene, sometimes paired with minor [100](001) and
696 [001](100) in orthopyroxene and [001](010) in the plagioclase. However, the dislocation
697 creep may have been too weak to erase the pre-existing CPO and would only have reduced
698 the magmatic fabric strength and the associated shape preferred orientation.

699 The metagabbro CXALV1 displays similar clinopyroxene and plagioclase CPO to that
700 observed in other mafic granulites (Figs. 8-11). However, it is characterised by large
701 deformed clinopyroxene and plagioclase grains surrounded by numerous small grains with no
702 subgrain and linear grain boundaries, which is a texture distinct from other samples (Figs. 10,
703 11). The large deformed clinopyroxene displays a depletion in LREE as well as observed in
704 the bulk rock, orthopyroxene and plagioclase grains (Supplementary Tables S1, S2;
705 Supplementary Fig. S3). This suggests that this sample recorded a partial melting event
706 contemporaneous with deformation. In addition, the high proportion of newly formed
707 clinopyroxene grains in this sample shows slightly different chemical compositions compared
708 to neighbouring large clinopyroxene grains, with low CaO and Mg# and high Al_2O_3 content in
709 clinopyroxene (Fig. 4). These grains also display a higher LREE contents compared to
710 clinopyroxene grain cores (Supplementary Fig. S3). This suggests that these newly formed
711 grains are the result of a high-temperature reequilibration with a small proportion of trapped
712 liquid, enhancing diffusion creep.

713

714 *Websterites*

715 Websterite samples CO10A1 and PM6C8 display weak or absent intragranular misorientation,
716 very rare subgrain boundaries and linear grain boundaries (Figs. 10, 11). Clinopyroxene CPO

patterns in both websterites CO10A1 and PM6C8 are also weak, with a concentration of [001] axes parallel to X and [010] parallel to Z, as observed in two mafic granulites (CXTRA1, CXAZN1), suggesting activation of the (010)[001] slip system (Fig. 8; SL-type, Helmstaedt *et al.*, 1972, Zhang *et al.*, 2006). In the websterite PM6C8, the [001](010) plagioclase fabric correlates with the pyroxenes fabric, with [001] axes parallel in the three phases. The orthopyroxene and clinopyroxene CPO fabrics are similar, with [001] axes parallel to X and [010] parallel to Z suggesting similar crystallisation conditions.

In websterite PM6C8, clinopyroxene low-angle misorientations axes are aligned with both [010] and [001] axes (Fig. 9), which may be related to the activation of the [001](010) slip system (Griffin *et al.*, 2022). The occurrence of [010] low-angle misorientation in orthopyroxene can be correlated with the activation of the [001](100) slip system, whereas the occurrence of [100] low-angle misorientation in plagioclase can be attributed to the [001](010) slip system (van der Werf *et al.*, 2017; Allard *et al.*, 2021). Thus, the slip systems that activate low-angle misorientations form a CPO similar to the general fabric observed at sample scale, which is more a result of a SPO, reflecting a cumulative texture. It would have been followed by only diffusion creep to equilibrate grains and erase the cumulative texture. Websterites display less evidence of plastic deformation than granulites, which could be attributed to the age of their protolith formation. It is possible that websterites protolith is younger than mafic granulite protoliths, which may have recorded deformation events prior to their ascent. In this scenario, the formation of the websterites could have occurred shortly before their ascent in the host magma, dated at 20-29 Ma and 1-2 Ma for Cerro Aznares and Comallo, respectively (Fig. 1). However, these differences could also be explained by mineralogy. Experiments and modelling indicate that at 1000°C, the clinopyroxene is stronger than plagioclase under stress conditions between 1 and 100 MPa, and at a strain rate < 10-7s-1 (Tullis *et al.,* 1991). Indeed, mafic granulites, containing a larger proportion of plagioclase

742 compared to websterites, could preferentially accommodate strain recorded in the NPM crust,
743 acting as a weaker phase compared to clinopyroxene under similar P-T conditions. At this
744 stage, it is not possible to distinguish between these two hypotheses.
745
746 **Pressure, temperature conditions and stability of the lower crust**
747 The investigated xenolith collection contains metagabbros, metagabbronorites and websterites
748 equilibrated in the orthopyroxene-bearing granulite metamorphic field (Fig. 7). More
749 specifically, orthopyroxene-clinopyroxene thermometry and pseudosection calculations
750 applied to both orthopyroxene-bearing mafic granulites and websterites yield paragenesis
751 stabilisation conditions ranging from 760-820°C at 7.2-7.9 kbar to 1000-1150°C at 9-10.8
752 kbar (Fig. 7). Therefore, the maximum depth recorded by these samples is estimated to be
753 between 32 and 37 km, which places the origin of the xenoliths in the lower crust of the NPM
754 (Fig. 13).
755 The orthopyroxene granulite stability field is bracketed by a thermal gradient ranging
756 between 28 and 31.5°C/km (Fig. 7b). Currently, evidence for lower crustal melting in the
757 NPM is lacking, such as the observation of a low-velocity zone at lower crust depth (e.g
758 Chmielowski *et al*., 1999) or the presence of leucosomes associated with low-Al content in
759 pyroxenes in granulite samples, as the pyroxenes in these samples are high-Al (Figs. 2, 4).
760 Therefore, the solidus temperature of mafic granulites represents the maximum temperature
761 that the lower crust of the NPM can reach. At high pressures (>8 kbar), the calculated solidus
762 temperature in the pseudosection is ~1180°C (Fig. 7a; Supplementary Fig. S4), which is
763 consistent with the known dry solidus temperature of mafic granulites (Bucher & Grapes,
764 2011). Based on our petrological inferred geotherm, this temperature is reached at a depth of
765 37.5-42 km (Fig. 7). The inferred depth for the emplacement of the mafic granulites is
766 interpreted as the depth of the petrological Moho. It is in agreement with the estimated Moho

depth of the NPM between 30 and 40 km, from recent gravity, seismic and tomographic studies (Van der Meijde *et al.*, 2013; Chulick *et al.*, 2013; Assumpção *et al.*, 2013). However, the study of Gomez Dacal *et al.* (2021) estimates in the NPM a deeper Moho located between 45 and 50 km, and a lower crustal geotherm that decreases from 29°C/km to less than 8°C/km. They show that in the NPM the thermal anomaly and the heating of the lithosphere occurred between 40 and 20 Ma, and that the cooling phase since then has been slow enough to maintain a similar gradient in the lithosphere until today. The studied xenoliths have been transported to the surface by 20 and 30 Ma lavas (Fig. 1), an age range that includes the global heating in the NPM. Furthermore, the unique Pleistocene xenolith (the websterite CO10A1 from Comallo) matches the P-T estimation range (7-8.8 kbar, 770-930°C; Fig. 7b) of all the other older xenoliths (i.e. Oligo-Miocene). Thus, the proposed NPM crustal geotherm has been constant since the Oligo-Miocene, and we cannot exclude that this geotherm may be stable beyond the Oligocene. Similarly, if the proposed maximum depth of origin of the studied granulites - based almost exclusively on Oligo-Miocene xenoliths - is comparable to today's geophysical Moho models (Van der Meijde *et al.*, 2013; Chulick *et al.*, 2013; Assumpção *et al.*, 2013), then the NPM crustal geotherm is stable beyond the Oligo-Miocene times and the last LIP event.

New constraints on the lower crust and the petrological Moho below the NPM

From the studied xenoliths, in NPM lower crust, the observed dislocation creep mechanisms and associated slip systems inferred from misorientation axes in different samples were the same, developing [001](100) with minor [100](001) in clinopyroxene (e.g. Raterron *et al.*, 1994), [001](100) in orthopyroxene (e.g. Jung *et al.*, 2010) and [001](010) in plagioclase (e.g. Kruse *et al.*, 2001; Figs. 8, 9). The infrequent plastic deformation witnessed

in the xenoliths occurred under P-T conditions of the orthopyroxene granulite facies, at 760-820°C at 7.2-7.9 kbar to 1000-1150°C at 9-10.8 kbar (Fig. 7).

The most recent significant compressive tectonic event affecting the NPM occurred during the Late Paleozoic (e.g. Von Gosen, 2009). If the protoliths of the investigated NPM lower crustal xenoliths were formed at that time, they should not have undergone significant plastic deformation to preserve their magmatic fabrics. However, if they are younger (Jurassic or Cenozoic), it has been evidenced that the Patagonian Triassic and Jurassic extension generated basins surrounding the NPM, yet preserved the latter from massive faulting (e.g. Renda *et al.*, 2019). Moreover, Aragón *et al.* (2011) proposed that the NPM remained undeformed by Cenozoic tectonics other than faulting and massive uplift, and designated the NPM as a rigid lithospheric block. The present microstructural analysis supports the view that the NPM lower crust remained underformed throughout the Cenozoic and, maybe to a maximum extent, since the end of the Late Paleozoic tectonic events.

The Petrologic Moho below the NPM can be considered as a significantly magmatic-influenced Moho, as the lower crust consists mainly of mafic granulites with magmatic protoliths, probably Cenozoic in age, even if we can not exclude Late Paleozoic to Jurassic ages for some of them (Fig. 13). Moreover, the lower crust does not record significant deformation events and both its composition and rheology appear homogeneous between 32

and 37 km depth. Recent magmatic activity continues to influence the relatively hot geotherm (about 30°C/km; Fig. 13).

CONCLUSIONS

- The North Patagonian Massif (NPM) lower crust is composed predominantly of a main plagioclase-clinopyroxene-orthopyroxene-spinel assemblage.
- Petrology, geochemistry and microstructures suggest that the mafic granulites and websterites have a magmatic protolith, possibly related to one of the magmatic events that have occurred in the NPM since the Permo-Trias, namely, the Permo-Trias Choiyoi silicic LIP, the Jurassic Chon Aike silicic LIP and the Oligo-Miocene LIP.
- The P-T conditions of the xenoliths were determined to be between 760-820°C at 7.2-7.9 kbar and 1000-1150°C at 9-10.8 kbar, defining an Oligocene-Pleistocene geotherm in the NPM crust of 28-31.5°C/km and a petrological Moho located at a depth of 37.5-42 km.
- The low-angle misorientation analysis reveals that dislocation creep developed through [001](100)/[100](001) slip system in clinopyroxene, [001](100) in orthopyroxene and [001](100) in plagioclase. However, the dislocation creep mechanisms did not erase the inherited magmatic CPO, which produced in both

827 clinopyroxene and orthopyroxene a [001](010) or [100](001) fabric, and a [100](010)
828 fabric in the plagioclase.
829 - The preservation of the magmatic fabrics in xenoliths suggests that the NPM lower
830 crust has been preserved from an intense tectonic event since the crystallisation of
831 magmatic protoliths.
832

833 **FUNDING**

834 This study has been partially supported through the French Ministry of Higher Education,
835 Research and Innovation PhD scholarship of N. Muckensturm, the grant EUR TESS N°ANR-
836 18-EURE-0018 in the framework of the Programme des Investissements d'Avenir and the
837 ISIFOR CaMaMiCu project.
838

839 **ACKNOWLEDGEMENTS**

840 We are grateful to Fabienne de Parseval for high-quality thin sections, Françoise Maubé for
841 assistance with SEM, Philippe De Parserval for assistance with Electron microprobe, Aurélie
842 Marquet for assistance with LA-ICPMS, and Arnaud Proietti for assistance with SEM-EBSD.

This manuscript was improved by constructive and thoughtful comments and reviews from editor Georg Zellmer and two reviewers, Marina Koreshkova and one anonymous.

DATA AVAILABILITY STATEMENT

The data underlying this article will be shared on reasonable request to the corresponding author.

REFERENCES

Afonso, J. C., Salajegheh, F., Szwillus, W., Ebbing, J. & Gaina, C. (2019). A global reference model of the lithosphere and upper mantle from joint inversion and analysis of multiple data sets. *Geophysical Journal International* **217**, 1602–1628.

Amiguet, E. (2009). Déformation expérimentale de diopside dans les conditions de pression et température du manteau supérieur. Université des Sciences et Technologies de Lille, 145 pp.

Allard, M., Ildefonse, B., Oliot, É. & Barou, F. (2021). Plastic Deformation of Plagioclase in Oceanic Gabbro Accreted at a Slow-Spreading Ridge (Hole U1473A, Atlantis Bank, Southwest Indian Ridge). *Journal of Geophysical Research: Solid Earth* **126**.

Aoki, K.I. & Kushiro, I. (1968). Some clinopyroxenes from ultramafic inclusions in Dreiser Weiher, Eifel. *Contributions to Mineralogy and Petrology* **18**, 326–337.

Aragón, E., D'Eramo, F., Castro, A., Pinotti, L., Brunelli, D., Rabbia, O., Rivalenti, G., Varela, R., Spakman, W., Demartis, M., Cavarozzi, C. E., Aguilera, Y. E., Mazzucchelli, M. & Ribot, A. (2011). Tectono-magmatic response to major convergence changes in the North

868 Patagonian suprasubduction system; the Paleogene subduction–transcurrent plate margin
869 transition. *Tectonophysics* **509**, 218–237.
870
871 Asiain, L., Florencia Gargiulo, M., Ferracutti, G., Hauser, N. & Bjerg, E. A. (2022). Evolution
872 of the volcanism in the northwestern part of meseta de Somuncurá, Patagonia, Argentina.
873 *Journal of South American Earth Sciences* **113**, 103653.
874
875 Assumpção, M., Feng, M., Tassara, A. & Julià, J. (2013). Models of crustal thickness for
876 South America from seismic refraction, receiver functions and surface wave tomography.
877 *Tectonophysics* **609**, 82–96.
878
879 Bachmann, F., Hielscher, R. & Schaeben, H. (2010). Texture Analysis with MTEX – Free and
880 Open Source Software Toolbox. *Solid State Phenomena* **160**, 63–68.
881
882 Bachmann, F., Hielscher, R. & Schaeben, H. (2011). Grain detection from 2d and 3d EBSD
883 data—Specification of the MTEX algorithm. *Ultramicroscopy* **111**, 1720–1733.
884
885 Beccaluva, L., Bianchini, G., Natali, C. & Siena, F. (2009). Continental Flood Basalts and
886 Mantle Plumes: a Case Study of the Northern Ethiopian Plateau. *Journal of Petrology* **50**,
887 1377–1403.
888
889 Bernard, R. E., Schulte-Pelkum, V. & Behr, W. M. (2021). The competing effects of olivine
890 and orthopyroxene CPO on seismic anisotropy. *Tectonophysics* **814**, 228954.
891
892 Bjerg, E. A., Ntaflos, T., Kurat, G., Dobosi, G. & Labudía, C. H. (2005). The upper mantle

893 beneath Patagonia, Argentina, documented by xenoliths from alkali basalts. *Journal of South*
894 *American Earth Sciences* **18**, 125–145.
895
896 Bjerg, E. A., Ntaflos, T., Thoni, M., Aliani, P. & Labudia, C. H. (2009). Heterogeneous
897 Lithospheric Mantle beneath Northern Patagonia: Evidence from Prahuaniyeu Garnet- and
898 Spinel-Peridotites. *Journal of Petrology* **50**, 1267–1298.
899
900 Bryan, S. E. & Ferrari, L. (2013). Large igneous provinces and silicic large igneous
901 provinces: Progress in our understanding over the last 25 years. *Geological Society of*
902 *America Bulletin* **125**, 1053–1078.
903
904 Bucher, K. & Grapes, R. (2011). *Petrogenesis of Metamorphic Rocks*. Berlin, Heidelberg:
905 Springer Berlin Heidelberg.
906
907 Bunge, H.J., (1982). Texture Analysis in Materials Science. Butterworth-Heinemann, London,
908 599 pp.
909
910 Castro, A., Aragón, E., Díaz-Alvarado, J., Blanco, I., García-Casco, A., Vogt, K. & Liu, D.-Y.
911 (2011). Age and composition of granulite xenoliths from Paso de Indios, Chubut province,
912 Argentina. *Journal of South American Earth Sciences* **32**, 567–574.
913
914 Cawood, P. A., Hawkesworth, C. J. & Dhuime, B. (2013). The continental record and the
915 generation of continental crust. *Geological Society of America Bulletin* **125**, 14–32.
916
917 Cawood, P. A., Chowdhury, P., Mulder, J. A., Hawkesworth, C. J., Capitanio, F. A.,

Gunawardana, P. M. & Nebel, O. (2022). Secular Evolution of Continents and the Earth System. *Reviews of Geophysics* **60**(4).

Christiansen, R. O., Gianni, G. M., Ballivián Justiniano, C. A., García, H. P. A. & Wohnlich, S. (2022). The role of geotectonic setting on the heat flow distribution of southern South America. *Geophysical Journal International* **230**, 1911–1927.

Chulick, G. S., Detweiler, S. & Mooney, W. D. (2013). Seismic structure of the crust and uppermost mantle of South America and surrounding oceanic basins. *Journal of South American Earth Sciences* **42**, 260–276.

Coltice, N., Husson, L., Faccenna, C. & Arnould, M. (2019). What drives tectonic plates? *Science Advances* **5**, eaax4295.

Cordenons, P. D., Remesal, M. B., Salani, F. M. & Cerredo, M. E. (2020). Temporal and spatial evolution of the Somún Curá Magmatic Province, Northern Extra-Andean Patagonia, Argentina. *Journal of South American Earth Sciences* **104**, 102881.

Daly, L., Piazolo, S., Lee, M. R., Griffin, S., Chung, P., Campanale, F., Cohen, B. E., Hallis, L. J., Trimby, P. W., Baumgartner, R., Forman, L. V. & Benedix, G. K. (2019).

938 Understanding the emplacement of Martian volcanic rocks using petrofabrics of the nakhlite
939 meteorites. *Earth and Planetary Science Letters* **520**, 220–230.
940
941 Dantas, C. (2007). Caractérisation du manteau supérieur patagonien: les enclaves
942 ultramafiques et mafiques dans les laves alcalines. Université de Toulouse III, 336 pp.
943
944 Desta, M. T., Ayalew, D., Ishiwatari, A., Arai, S. & Tamura, A. (2014). Ferropicrite from the
945 Lalibela area in the Ethiopian large igneous province. *Journal of Mineralogical and*
946 *Petrological Sciences* **109**, 191–207.
947
948 Falco, J. I., Hauser, N., Scivetti, N., Reimold, W. U., Schmitt, R. T. & Folguera, A. (2022).
949 Upper Triassic to Middle Jurassic magmatic evolution of northern Patagonia: Insights from
950 the tectonic and crustal evolution of the Los Menucos area, North Patagonian Massif,
951 Argentina. *Journal of South American Earth Sciences* **113**, 103631.
952
953 Frets, E., Tommasi, A., Garrido, C. J., Padrón-Navarta, J. A., Amri, I. & Targuisti, K. (2012).
954 Deformation processes and rheology of pyroxenites under lithospheric mantle conditions.

Journal of Structural Geology **39**, 138–157.

Fuhrman, M. L. & Lindsley, D. H. (1988). Ternary-feldspar modeling and thermometry. *American Mineralogist* **73**, 201–215.

Fujimaki, H., Tatsumoto, M. and Aoki, K.-i. (1984). Partition coefficients of Hf, Zr, and REE between phenocrysts and groundmasses. *Journal of Geophysical Research* **89**, 662-672.

Gianni, G. M. & Navarrete, C. R. (2022). Catastrophic slab loss in southwestern Pangea preserved in the mantle and igneous record. *Nature Communications* **13**, 698.

Gómez Dacal, M. L., Scheck-Wenderoth, M., Aragón, E., Bott, J., Cacace, M. & Tocho, C. (2021). Unravelling the lithospheric-scale thermal field of the North Patagonian Massif plateau (Argentina) and its relations to the topographic evolution of the area. *International Journal of Earth Sciences* **110**, 2315–2331.

Gómez Dacal, M. L., Tocho, C., Aragón, E., Sippel, J., Scheck-Wenderoth, M. & Ponce, A. (2017). Lithospheric 3D gravity modelling using upper-mantle density constraints: Towards a characterization of the crustal configuration in the North Patagonian Massif area, Argentina. *Tectonophysics* **700–701**, 150–161.

Govindaraju, K. (1989). 1989 Compilation of working values and sample description for 272 geostandards. *Geostandards Newsletter* **13**, 1–113.

Green, E. C. R., White, R. W., Diener, J. F. A., Powell, R., Holland, T. J. B. & Palin, R. M.

(2016). Activity-composition relations for the calculation of partial melting equilibria in metabasic rocks. *Journal of Metamorphic Geology* **34**, 845–869.

Griffin, S., Daly, L., Piazolo, S., Forman, L. V., Cohen, B. E., Lee, M. R., Trimby, P. W., Baumgartner, R. J., Benedix, G. K. & Hoefnagels, B. (2022). Can the Magmatic Conditions of the Martian Nakhlites be Discerned via Investigation of Clinopyroxene and Olivine Intracrystalline Misorientations? *Journal of Geophysical Research: Planets* **127**.

Griffin, W., Powell, W., Pearson, N. J. & O'Reilly, S. (2008). GLITTER: data reduction software for laser ablation ICP-MS. *Short Course Series* **40**, 308–311.

Hacker, B. R., Kelemen, P. B. & Behn, M. D. (2015). Continental Lower Crust. *Annual Review of Earth and Planetary Sciences* **43**, 167–205.

Helmstaedt, H., Anderson, O. L., & Gavasci, A. T. (1972). Petrofabric studies of eclogite, spinel-Websterite, and spinel-lherzolite Xenoliths from kimberlite-bearing breccia pipes in southeastern Utah and northeastern Arizona. *Journal of Geophysical Research* **77**(23), 4350-4365.

Holland, T. J. B. & Powell, R. (2004). An internally consistent thermodynamic data set for phases of petrological interest: an internally consistent thermodynamic data set. *Journal of Metamorphic Geology* **16**, 309–343.

Holland, T. J. B. & Powell, R. (2011). An improved and extended internally consistent thermodynamic dataset for phases of petrological interest, involving a new equation of state

for solids: thermodynamic dataset for phases of petrological interest. *Journal of Metamorphic Geology* **29**, 333–383.

Idárraga-García, J. & Vargas, C. A. (2018). Depth to the bottom of magnetic layer in South America and its relationship to Curie isotherm, Moho depth and seismicity behaviour. *Geodesy and Geodynamics* **9**, 93–107.

Jacques, G., Hoernle, K., Gill, J., Wehrmann, H., Bindeman, I. & Lara, L. E. (2014). Geochemical variations in the Central Southern Volcanic Zone, Chile (38–43°S): The role of fluids in generating arc magmas. *Chemical Geology* **371**, 27–45.

Jochum, K. P., Weis, U., Stoll, B., Kuzmin, D., Yang, Q., Raczek, I., Jacob, D. E., Stracke, A., Birbaum, K., Frick, D. A., Günther, D. & Enzweiler, J. (2011). Determination of Reference Values for NIST SRM 610-617 Glasses Following ISO Guidelines. *Geostandards and Geoanalytical Research* **35**, 397–429.

Jung, H., Park, M., Jung, S., & Lee, J. (2010). Lattice preferred orientation, water content, and

seismic anisotropy of orthopyroxene. *Journal of Earth Science*, ***21***(5), 555-568.

Kay, S. M., Gorring, M. & Ramos, V. A. (2004). Magmatic sources, setting and causes of Eocene to Recent Patagonian plateau magmatism (36°S to 52°S latitude). *Revista de la Asociación Geológica Argentina* **59**(4), 556-568.

Kay, S. M., Ardolino, A. A., Gorring, M. L. & Ramos, V. A. (2007). The Somuncura Large Igneous Province in Patagonia: Interaction of a Transient Mantle Thermal Anomaly with a Subducting Slab. *Journal of Petrology* **48**, 43–77.

Kempton, P. D. & Harmon, R. S. (1992). Oxygen isotope evidence for large-scale hybridization of the lower crust during magmatic underplating. *Geochimica et Cosmochimica Acta* **56**, 971–986.

Kourim, F., Vauchez, A., Bodinier, J.-L., Alard, O. & Bendaoud, A. (2015). Subcontinental lithosphere reactivation beneath the Hoggar swell (Algeria): Localized deformation, melt channeling and heat advection. *Tectonophysics* **650**, 18–33.

Kruse, R., Stünitz, H., & Kunze, K. (2001). Dynamic recrystallization processes in plagioclase porphyroclasts. *Journal of Structural Geology*, ***23***(11), 1781-1802.

Lee, W., Lee, H., Kim, D., Kim, J., Oh, J., Song, J.-H., Kim, C. H., Park, C. H. & Stuart, F. M. (2021). Trace element and helium isotope geochemistry of the Cenozoic intraplate volcanism in the East Sea (Sea of Japan): Implications for lithosphere-asthenosphere

1046 interaction. *Lithos* **388–389**, 106075.
1047
1048 López De Luchi, M. G. & Rapalini, A. E. (2002). Middle Jurassic dyke swarms in the North
1049 Patagonian Massif: the Lonco Trapial Formation in the Sierra de Mamil Choique, Río Negro
1050 province, Argentina. *Journal of South American Earth Sciences* **15**, 625–641.
1051
1052 Luppo, T., López de Luchi, M. G., Rapalini, A. E., Martínez Dopico, C. I. & Fanning, C. M.
1053 (2018). Geochronologic evidence of a large magmatic province in northern Patagonia
1054 encompassing the Permian-Triassic boundary. *Journal of South American Earth Sciences* **82**,
1055 346–355.
1056
1057 Mallmann, G. (2004). Processos e Componentes Mantélicos no Norte da Patagônia
1058 (Argentina) e Relações com a Subducção Andina: Evidências Petrográficas, Geoquímicas e
1059 Isotópicas em Xenólitos Ultramáficos Mantélicos. Universidade Federal do Rio Grande do
1060 Sul Instituto de Geociências, 102 pp.
1061
1062 Martínez Dopico, C. I., López de Luchi, M. G., Rapalini, A. E. & Kleinhanns, I. C. (2011).
1063 Crustal segments in the North Patagonian Massif, Patagonia: An integrated perspective based
1064 on Sm–Nd isotope systematics. *Journal of South American Earth Sciences* **31**, 324–341.
1065
1066 Martínez Dopico, C. I., López De Luchi, M. G., Rapalini, A. E., Fanning, C. M. & Antonio,
1067 P. Y. J. (2019). Geochemistry and geochronology of the shallow-level La Esperanza
1068 magmatic system (Permian-Triassic), Northern Patagonia. *Journal of South American Earth*

Sciences **96**, 102347.

Massaferro, G. I., Haller, M. J., Dostal, J., Pécskay, Z., Prez, H., Meister, C. & Alric, V. (2014). Possible sources for monogenetic Pliocene–Quaternary basaltic volcanism in northern Patagonia. *Journal of South American Earth Sciences* **55**, 29–42.

McCoy-West, A. J., Baker, J. A., Faure, K. & Wysoczanski, R. (2010). Petrogenesis and Origins of Mid-Cretaceous Continental Intraplate Volcanism in Marlborough, New Zealand: Implications for the Long-lived HIMU Magmatic Mega-province of the SW Pacific. *Journal of Petrology* **51**, 2003–2045.

McDonough, W. F. & Sun, S. -s. (1995). The composition of the Earth. *Chemical Geology* **120**, 223–253.

Melchiorre, M., Faccini, B., Grégoire, M., Benoit, M., Casetta, F. & Coltorti, M. (2020). Melting and metasomatism/refertilisation processes in the Patagonian sub-continental lithospheric mantle: A review. *Lithos* **354–355**, 105324.

Mengel, K. & Kern, H. (1992). Evolution of the petrological and seismic Moho-implications for the continental crust-mantle boundary. *Terra Nova* **4**, 109–116.

Mouthereau, F., Angrand, P., Jourdon, A., Ternois, S., Fillon, C., Calassou, S., Chevrot, S., Ford, M., Jolivet, L., Manatschal, G., Masini, E., Thinon, I., Vidal, O. & Baudin, T. (2021). Cenozoic mountain building and topographic evolution in Western Europe: impact of billions of years of lithosphere evolution and plate kinematics. *BSGF - Earth Sciences Bulletin* **192**,

56.

Mundl, A., Ntaflos, T., Ackerman, L., Bizimis, M., Bjerg, E. A., Wegner, W. & Hauzenberger, C. A. (2016). Geochemical and Os–Hf–Nd–Sr Isotopic Characterization of North Patagonian Mantle Xenoliths: Implications for Extensive Melt Extraction and Percolation Processes. *Journal of Petrology* **57**, 685–715.

Navarrete, C., Gianni, G., Encinas, A., Márquez, M., Kamerbeek, Y., Valle, M. & Folguera, A. (2019). Triassic to Middle Jurassic geodynamic evolution of southwestern Gondwana: From a large flat-slab to mantle plume suction in a rollback subduction setting. *Earth-Science Reviews* **194**, 125–159.

Navarrete, C., Gianni, G., Massaferro, G. & Butler, K. (2020). The fate of the Farallon slab beneath Patagonia and its links to Cenozoic intraplate magmatism, marine transgressions and topographic uplift. *Earth-Science Reviews* **210**, 103379.

Natali, C., Beccaluva, L., Bianchini, G., Ellam, R. M., Savo, A., Siena, F. & Stuart, F. M. (2016). High-MgO lavas associated to CFB as indicators of plume-related thermochemical effects: The case of ultra-titaniferous picrite–basalt from the Northern Ethiopian–Yemeni Plateau. *Gondwana Research* **34**, 29–48.

O'Reilly, S. Y. & Griffin, W. L. (2013). Moho vs crust–mantle boundary: Evolution of an idea. *Tectonophysics* **609**, 535–546.

Oriolo, S., González, P. D., Renda, E. M., Basei, M. A. S., Otamendi, J., Cordenons, P.,

Marcos, P., Yoya, M. B., Ballivián Justiniano, C. A. & Suárez, R. (2023). Linking accretionary orogens with continental crustal growth and stabilization: Lessons from Patagonia. *Gondwana Research* **121**, 368–382.

Pankhurst, R. J. & Rapela, C. R. (1995). Production of Jurassic rhyolite by anatexis of the lower crust of Patagonia. *Earth and Planetary Science Letters* **134**, 23–36.

Pankhurst, R. J., Leat, P. T., Sruoga, P., Rapela, C. W., Márquez, M., Storey, B. C. & Riley, T. R. (1998). The Chon Aike province of Patagonia and related rocks in West Antarctica: A silicic large igneous province. *Journal of Volcanology and Geothermal Research* **81**, 113–136.

Pankhurst, R. J., Rapela, C. W., Fanning, C. M. & Márquez, M. (2006). Gondwanide continental collision and the origin of Patagonia. *Earth-Science Reviews* **76**, 235–257.

Pankhurst, R. J., Rapela, C. W., López De Luchi, M. G., Rapalini, A. E., Fanning, C. M. & Galindo, C. (2014). The Gondwana connections of northern Patagonia. *Journal of the Geological Society* **171**, 313–328.

Passchier, C. W. & Trouw, R. A. J. (2005). *Microtectonics*. Berlin Heidelberg: Springer.

Ramos, V. A. (2008). Patagonia: A paleozoic continent adrift? *Journal of South American Earth Sciences* **26**, 235–251.

Rapalini, A. E., De Luchi, M. L., Tohver, E. & Cawood, P. A. (2013). The South American

1144 ancestry of the North Patagonian Massif: geochronological evidence for an autochthonous
1145 origin? *Terra Nova* **25**, 337–342.
1146
1147 Rapela, C. W. & Pankhurst, R. J. (2020). The Continental Crust of Northeastern Patagonia.
1148 *Ameghiniana* **57**.
1149
1150 Raterron, P., Doukhan, N., Jaoul, O. & Doukhan, J. C. (1994). High temperature deformation
1151 of diopside IV: predominance of {110} glide above 1000°C. *Physics of the Earth and*
1152 *Planetary Interiors* **82**, 209–222.
1153
1154 Renda, E. M., Alvarez, D., Prezzi, C., Oriolo, S. & Vizán, H. (2019). Inherited basement
1155 structures and their influence in foreland evolution: A case study in Central Patagonia,
1156 Argentina. *Tectonophysics* **772**, 228232.
1157
1158 Rudnick, R. L. & Fountain, D. M. (1995). Nature and composition of the continental crust: A
1159 lower crustal perspective. *Reviews of Geophysics* **33**, 267.
1160
1161 Schilling, M. E., Carlson, R. W., Conceição, R. V., Dantas, C., Bertotto, G. W. & Koester, E.
1162 (2008). Re–Os isotope constraints on subcontinental lithospheric mantle evolution of southern

South America. *Earth and Planetary Science Letters* **268**, 89–101.

Schilling, M. E., Carlson R.W., Tassara A., Conceição R.V., Bertotto G.W., Vásquez M., Muñoz D., Jalowitzki T., Gervasoni F., Morata D. (2017). The origin of Patagonia revealed by Re-Os systematics of mantle xenoliths. *Precambrian Research* **294**, 15–32.

Soret, M., Agard, P., Ildefonse, B., Dubacq, B., Prigent, C. & Rosenberg, C. (2019). Deformation mechanisms in mafic amphibolites and granulites: record from the Semail metamorphic sole during subduction infancy. *Solid Earth* **10**, 1733–1755.

Stern, C. R., Frey, F. A., Futa, K., Zartman, R. E., Peng, Z. & Kurtis Kyser, T. (1990). Trace-element and Sr, Nd, Pb, and O isotopic composition of Pliocene and Quaternary alkali basalts of the Patagonian Plateau lavas of southernmost South America. *Contributions to Mineralogy and Petrology* **104**, 294–308.

Sun, P., Niu, Y., Guo, P., Duan, M., Wang, X. & Gong, H. (2022). Sublithosphere Mantle Crystallization and Immiscible Sulfide Melt Segregation in Continental Basalt Magmatism: Evidence from Clinopyroxene Megacrysts in the Cenozoic Basalts of Eastern China. *Journal*

of Petrology **63**, egac001.

Skemer, P., Katayama, I., Jiang, Z. & Karato, S. (2005). The misorientation index: Development of a new method for calculating the strength of lattice-preferred orientation. *Tectonophysics* **411**, 157–167.

Taufner, R., Viegas, G., Faleiros, F. M., Castellan, P. & Silva, R. (2021). Deformation mechanisms of granulite-facies mafic shear zones from hole U1473A, Atlantis Bank, Southwest Indian Ridge (IODP Expedition 360). *Journal of Structural Geology* **149**, 104380.

Tullis, T. E., Horowitz, F. G. & Tullis, J. (1991). Flow laws of polyphase aggregates from end-member flow laws. *Journal of Geophysical Research: Solid Earth* **96**, 8081–8096.

van der Meijde, M., Julià, J. & Assumpção, M. (2013). Gravity derived Moho for South America. *Tectonophysics* **609**, 456–467.

van der Werf, T., Chatzaras, V., Kriegsman, L. M., Kronenberg, A., Tikoff, B. & Drury, M. R. (2017). Constraints on the rheology of the lower crust in a strike-slip plate boundary: evidence from the San Quintín xenoliths, Baja California, Mexico. *Solid Earth* **8**, 1211–1239.

Van Achterbergh, E., Ryan, C. G., Jackson, S. E. & Griffin, W. L. (2001). Data Reduction for LA-ICPMS. In: Sylvester, P. (ed.) *Laser-ablation-ICPMS in the Earth Sciences: Principles and Applications.* Ottawa, Ontario: Mineralogical Association of Canada. 239-243.

Von Gosen, W. (2009). Stages of Late Palaeozoic deformation and intrusive activity in the

western part of the North Patagonian Massif (southern Argentina) and their geotectonic implications. *Geological Magazine* **146**, 48–71.

Wang, Y. F., Zhang, J. F., Jin, Z. M. & Green, H. W. (2012). Mafic granulite rheology: Implications for a weak continental lower crust. *Earth and Planetary Science Letters* **353–354**, 99–107.

Wells, P. R. A. (1977). Pyroxene thermometry in simple and complex systems. *Contributions to Mineralogy and Petrology* **62**, 129–139.

White, R. W., Powell, R. & Clarke, G. L. (2002). The interpretation of reaction textures in Fe-rich metapelitic granulites of the Musgrave Block, central Australia: constraints from mineral equilibria calculations in the system K2O-FeO-MgO-Al2O3-SiO2-H2O-TiO2-Fe2O3: reaction textures, musgrave block granulites. *Journal of Metamorphic Geology* **20**, 41–55.

White, R. W., Powell, R., Holland, T. J. B., Johnson, T. E. & Green, E. C. R. (2014). New mineral activity-composition relations for thermodynamic calculations in metapelitic systems. *Journal of Metamorphic Geology* **32**, 261–286.

Zaffarana, C., Lagorio, S., Orts, D., Busteros, A., Nieto, D. S., Giacosa, R., Ruiz González, V., Boltshauser, B., Puigdomenech Negre, C., Somoza, R. & Haller, M. (2019). First geochemical and geochronological characterization of Late Cretaceous mesosilicic

magmatism in Gastre, Northern Patagonia, and its tectonic relation to other coeval volcanic rocks in the region. *Geological Magazine* **156**, 1285–1294.

Zaffarana, C. B., Lagorio, S. L., Gallastegui, G., Wörner, G., Orts, D. L., Gregori, D., Poma, S., Busteros, A., Giacosa, R., Silva Nieto, D., Ruiz González, V., Boltshauser, B., Puigdomenech Negre, C. & Haller, M. (2020). Petrogenetic study of the Lonco Trapial volcanism and its comparison with the Early-Middle Jurassic magmatic units from northern Patagonia. *Journal of South American Earth Sciences* **101**, 102624.

Zhang, J., Green II, H. W., & Bozhilov, K. N. (2006). Rheology of omphacite at high temperature and pressure and significance of its lattice preferred orientations. *Earth and Planetary Science Letters*, ***246***(3-4), 432-443.

FIGURE CAPTIONS

Fig. 1. Simplified geological map of the North Patagonian Massif, with its setting in Patagonia, based on SegemAR maps, after Pankhurst *et al.* (2014), Cordenons *et al.* (2020), Zaffarana *et al.* (2020) and Falco *et al.* (2022). Nq: Neuquen basin, Co: Colorado basin, NPM: North Patagonian Massif, CA: Cañadon Asfalto basin, SJo: San Jorge basin, DM: Deseado Massif.

Fig. 2. Photomicrographs of north Patagonian lower crustal xenoliths. (a) Spinel metagabbronorite (sample CXTRA4) under cross-polarized light; note conical albite twinning in plagioclase crystals. (b) Titanomagnetite metagabbro (sample CXCHE3) under plane-polarized light. (c) Titanomagnetite and olivine metagabbronorite (sample CXAZN1) under plane-polarized light. Note clinopyroxene spongious rim highlighted by red boxes. (d)

Ferrian-pleonaste and Al-magnetite relations in metagabbro CXALV1, under backscattered electrons. (e) Compositional layering in metagabbro CXALV1, under plane-polarized light. (f) CXCHE2 metagabbro under plane-polarized light. (g) Spinel websterite (sample PM6C8) under cross-polarized light.

Fig. 3. Bulk rock Mg# vs. SiO_2/Al_2O_3 plotted in the granulite classification of Kempton & Harmon (1992). Primitive basalt field and differentiation trends are from the same authors. North Patagonian Cenozoic lavas field is from Kay *et al.* (2004, 2007), Jacques *et al.* (2014), Massaferro *et al.* (2014) and Asiain *et al.* (2022). Granulite compositions from Pankhurst & Rapela (1995; Sierra de los Chacays, southern NPM) and Castro *et al.* (2011; Pasos de Indios, Cañadon Asfalto basin) are added for comparison.

Fig. 4. Major element diagrams of clinopyroxene. (a) Ternary wollastonite-enstatite-hedenbergite plot of pyroxenes. (b) Plot of Al_{VI} *vs.* Al_{IV}. Compositional fields are from Aoki & Kushiro (1968). Al_{IV} = 2-(Si+Ti), molar; $Al_{VI} = Al_{tot}-Al_{IV}$, molar. (c) Plot of Al_2O_3 vs Mg#. (d) Plot of Al_2O_3 vs TiO_2. Mg # = 100 x Mg/(Mg+Fet), molar.

Fig. 5. Major element diagrams of orthopyroxene and plagioclase. (a) Plot of Cr_2O_3 vs Mg# of orthopyroxene. (b) Plot of Al_2O_3 vs Mg# of orthopyroxene. (c) Detailed wollastonite-enstatite-hedenbergite ternary plot of pyroxene. (d) Detailed orthoclase-albite-anorthite ternary plot of feldspar.

Fig. 6. Rare earth and trace elements patterns of clinopyroxene normalized to chondrite. (a) REE patterns of north Patagonian granulite xenoliths. (b) Trace elements patterns. Chondrite

values are from McDonough & Sun (1995). Symbols and full lines represent analysis means while faded areas represent ranges of all analyses (see Table 3 for number of analyses).

Fig. 7. Estimated temperature and pressure of granulite xenoliths. (a) Calculated P-T pseudosection for sample CXTRA4, with contoured modal proportions for orthopyroxene and clinopyroxene. As they did not add precisions to the P-T stability field determination, the plagioclase and spinel modal were not contoured to make the figure readable. (b) P-T diagram combining the results of all thermometer and pseudosection calculations. The granulite stability fields shown correspond to an average of the stability fields of all the concerned samples.

Fig. 8. Crystallographic preferred orientation of clinopyroxene and orthopyroxene of analysed metagabbros, metagabbronorites and websterites. When detected, compositional layering is tagged and pole figures are rotated as the layering normal to Z. N is the number of grains and the strength is represented by J-index and M-index. The rainbow scale represents the mud (multiply uniform density).

Fig. 9. (a) Crystallographic preferred orientation of plagioclase. N is the number of grains, the strength is represented by J-index and M- index. Sample CXCHE2 was not contoured because the CPO pattern is saturated by multiplied very coarse grains. (b) Rotation axes accommodating low angle (2-10°) misorientations in clinopyroxene, orthopyroxene and plagioclase grains. Data is represented in inverse pole figures where the legend can be found in (c). N is the number of pixels plotted.

Fig. 10. Maps of intragranular deformation relative to the mean orientation of the grains for (a) clinopyroxene and (b) orthopyroxene. Deep blue grains are undeformed while the intragranular deformation is strong in green to red areas. Light blue grains are orthopyroxene, light orange is clinopyroxene, light yellow is plagioclase and light pink is spinel. (c) Normalized histograms representing clinopyroxene and orthopyroxene area proportions vs. misorientation angles (>1°) relative to mean grain orientations.

Fig. 11. (a) Plagioclase maps of intragranular deformation relative to the mean orientation of the grains. Deep blue plagioclase grains are undeformed while the intragranular deformation is strong in green to red areas. Light blue grains are orthopyroxene, light orange is clinopyroxene, light pink is spinel and light green is olivine. (b) Normalized histograms representing plagioclase area proportion vs. misorientation angles (>1°) relative to mean grain orientations.

Fig. 12. Calculated normalised tholeiitic basalts in equilibrium with clinopyroxene. Oligo-Miocene and Quaternary REE volcanic compositions in the vicinity of the studied xenoliths are plotted (from Stern *et al.*, 1990; Kay *et al.*, 2004, 2007; Jacques *et al.*, 2014; Massaferro *et al.*, 2014; Asiain *et al.*, 2022).

Fig. 13. (a) Estimated Cenozoic- to Quaternary-geotherm of the North Patagonian Massif and the associated lithologic section of the lithosphere between 0 and 60 km. (b) Simplified lithospheric section until 60 km in depth. The Moho is located around 32 km deep and displays an accumulation of all ages granulite lenses and websterites. The occurrence of depleted and re-fertilized peridotites and peridotite cumulates is from Mundle *et al.* (2016).

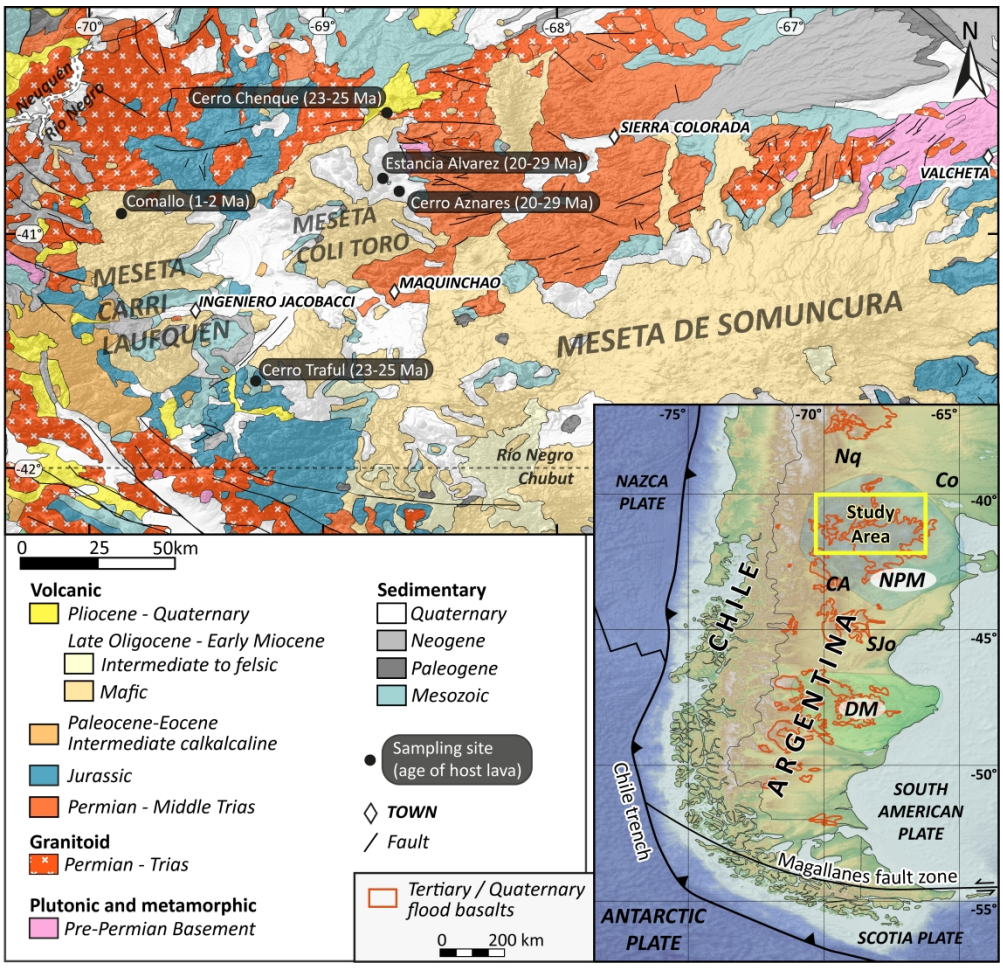

Fig. 1. Simplified geological map of the North Patagonian Massif, with its setting in Patagonia, based on SegemAR maps, after Pankhurst et al. (2014), Cordenons et al. (2020), Zaffarana et al. (2020) and Falco et al. (2022). Nq: Neuquen basin, Co: Colorado basin, NPM: North Patagonian Massif, CA: Cañadon Asfalto basin, SJo: San Jorge basin, DM: Deseado Massif.

170x163mm (600 x 600 DPI)

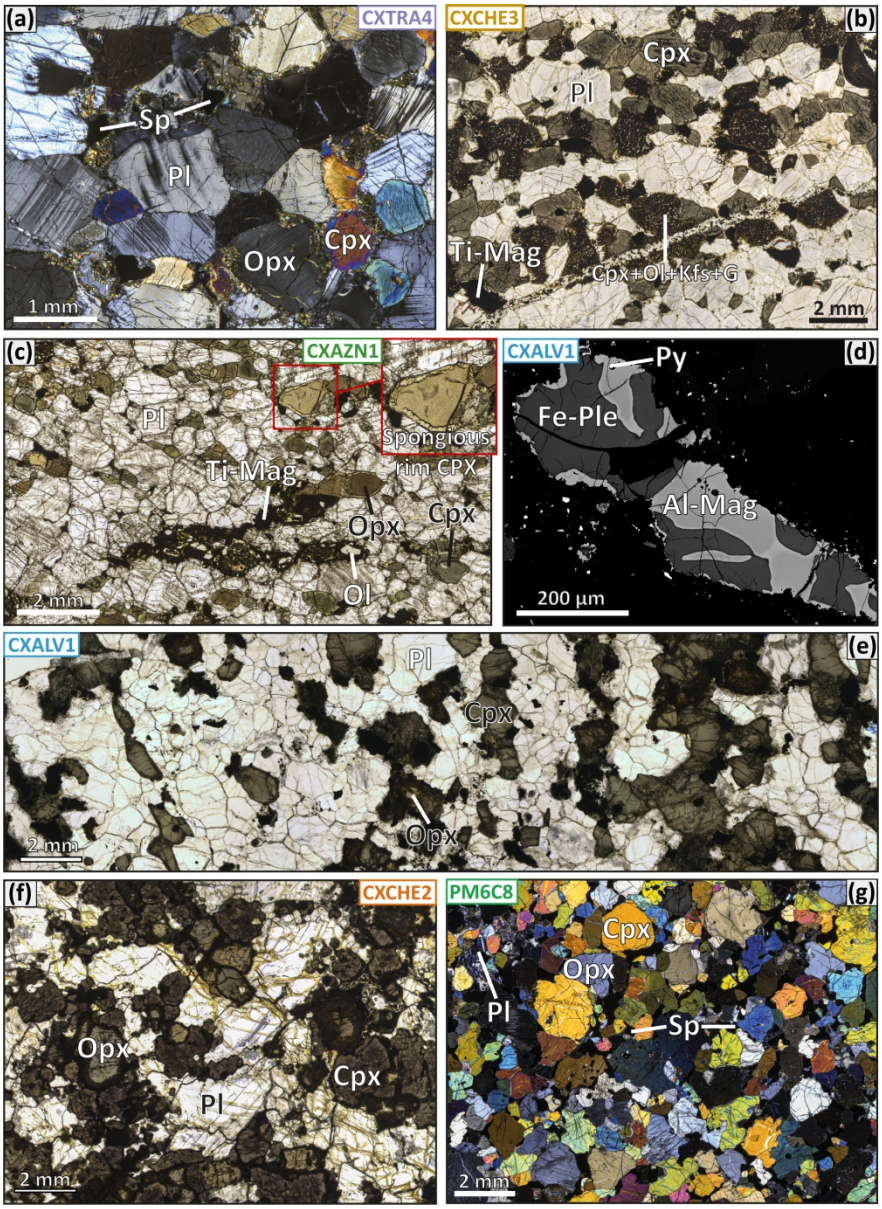

Fig. 2. Photomicrographs of north Patagonian lower crustal xenoliths. (a) Spinel metagabbronorite (sample CXTRA4) under cross-polarized light; note conical albite twinning in plagioclase crystals. (b) Titanomagnetite metagabbro (sample CXCHE3) under plane-polarized light. (c) Titanomagnetite and olivine metagabbronorite (sample CXAZN1) under plane-polarized light. Note clinopyroxene spongious rim highlighted by red boxes. (d) Ferrian-pleonaste and Al-magnetite relations in metagabbro CXALV1, under backscattered electrons. (e) Compositional layering in metagabbro CXALV1, under plane-polarized light. (f) CXCHE2 metagabbro under plane-polarized light. (g) Spinel websterite (sample PM6C8) under cross-polarized light.

170x233mm (300 x 300 DPI)

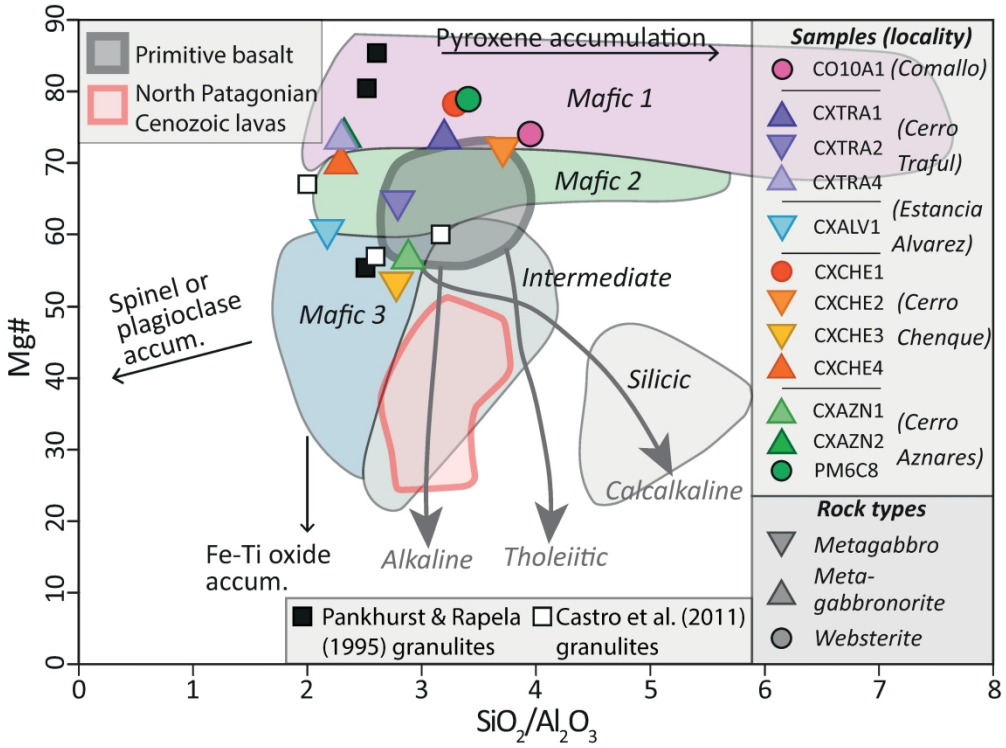

Fig. 3. Bulk rock Mg# vs. SiO2/Al2O3 plotted in the granulite classification of Kempton & Harmon (1992). Primitive basalt field and differentiation trends are from the same authors. North Patagonian Cenozoic lavas field is from Kay et al. (2004, 2007), Jacques et al. (2014), Massaferro et al. (2014) and Asiain et al. (2022). Granulite compositions from Pankhurst & Rapela (1995; Sierra de los Chacays, southern NPM) and Castro et al. (2011; Pasos de Indios, Cañadon Asfalto basin) are added for comparison.

170x127mm (600 x 600 DPI)

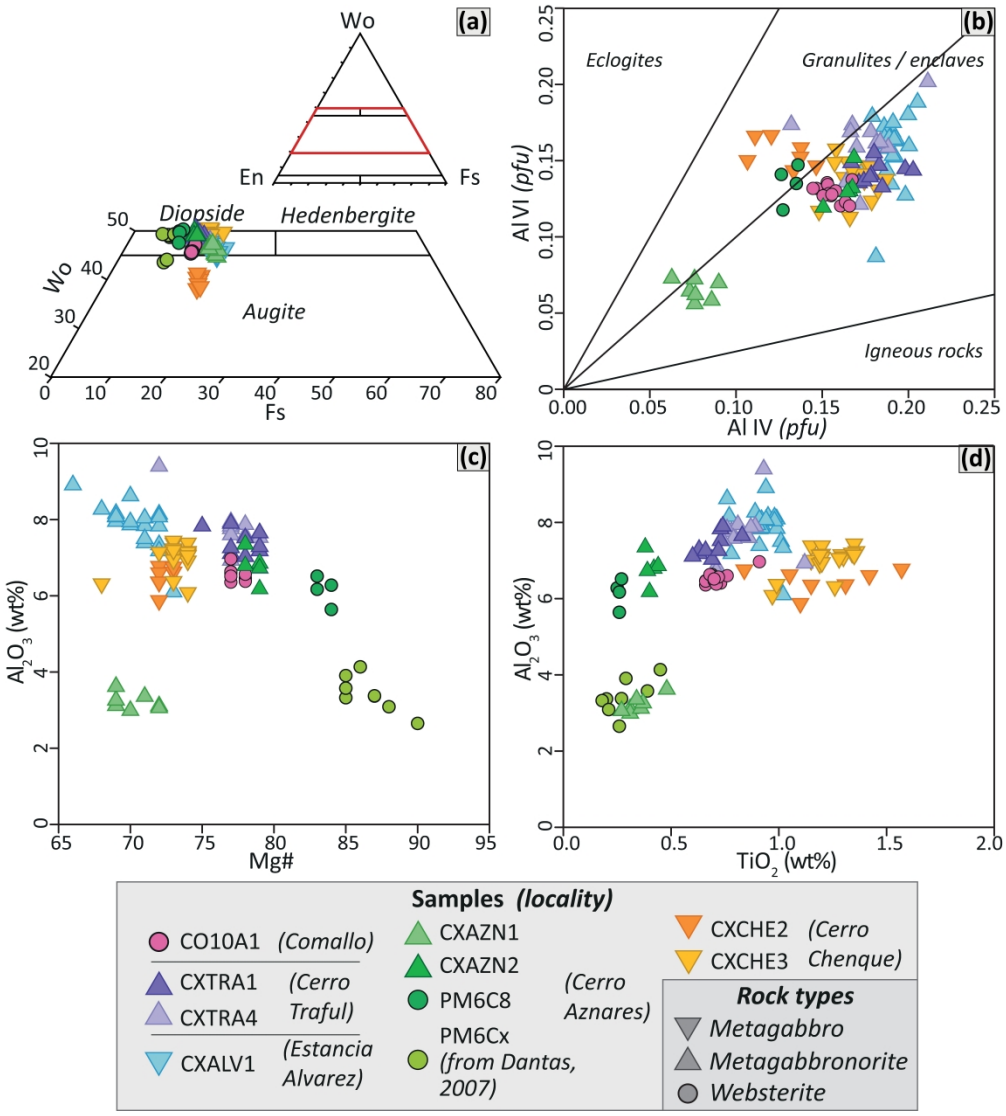

Fig. 4. Major element diagrams of clinopyroxene. (a) Ternary wollastonite-enstatite-hedenbergite plot of pyroxenes. (b) Plot of AlVI vs. AlIV. Compositional fields are from Aoki & Kushiro (1968). AlIV = 2-(Si+Ti), molar; AlVI = Altot-AlIV, molar. (c) Plot of Al2O3 vs Mg#. (d) Plot of Al2O3 vs TiO2. Mg # = 100 x Mg/(Mg+Fet), molar.

443x491mm (600 x 600 DPI)

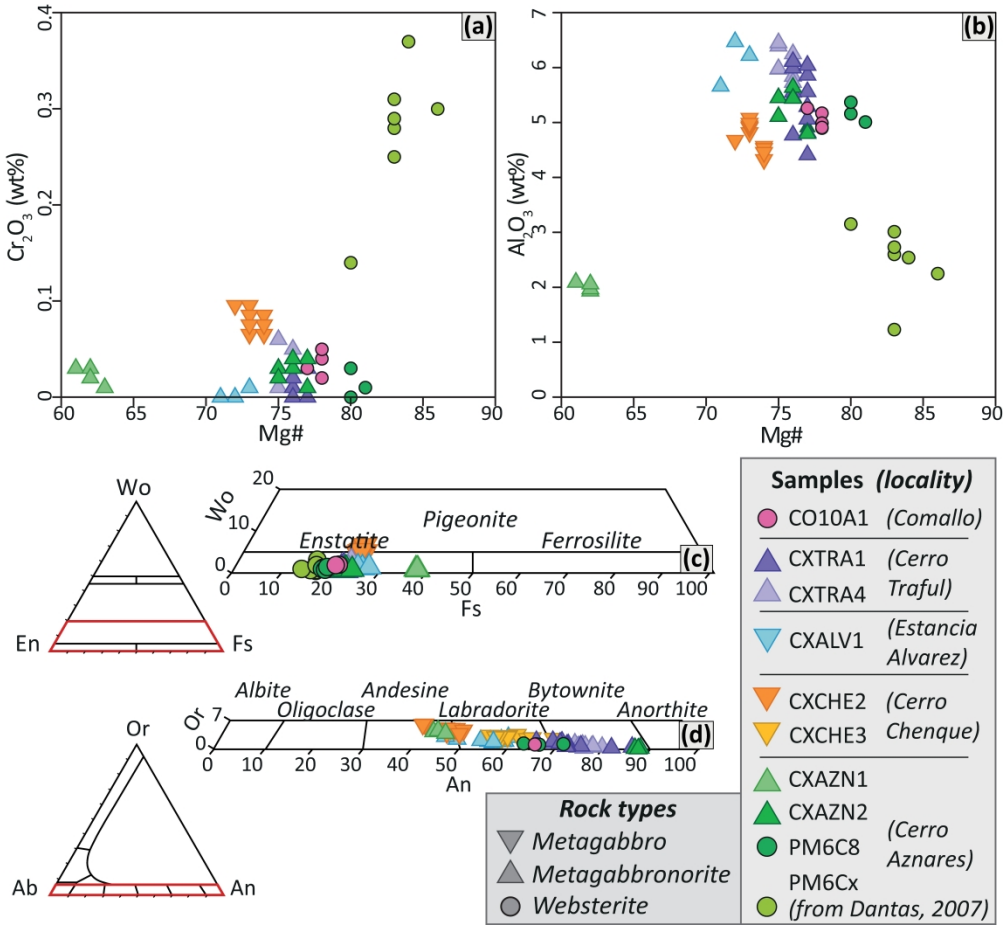

Fig. 5. Major element diagrams of orthopyroxene and plagioclase. (a) Plot of Cr2O3 vs Mg# of orthopyroxene. (b) Plot of Al2O3 vs Mg# of orthopyroxene. (c) Detailed wollastonite-enstatite-hedenbergite ternary plot of pyroxene. (d) Detailed orthoclase-albite-anorthite ternary plot of feldspar.

444x408mm (600 x 600 DPI)

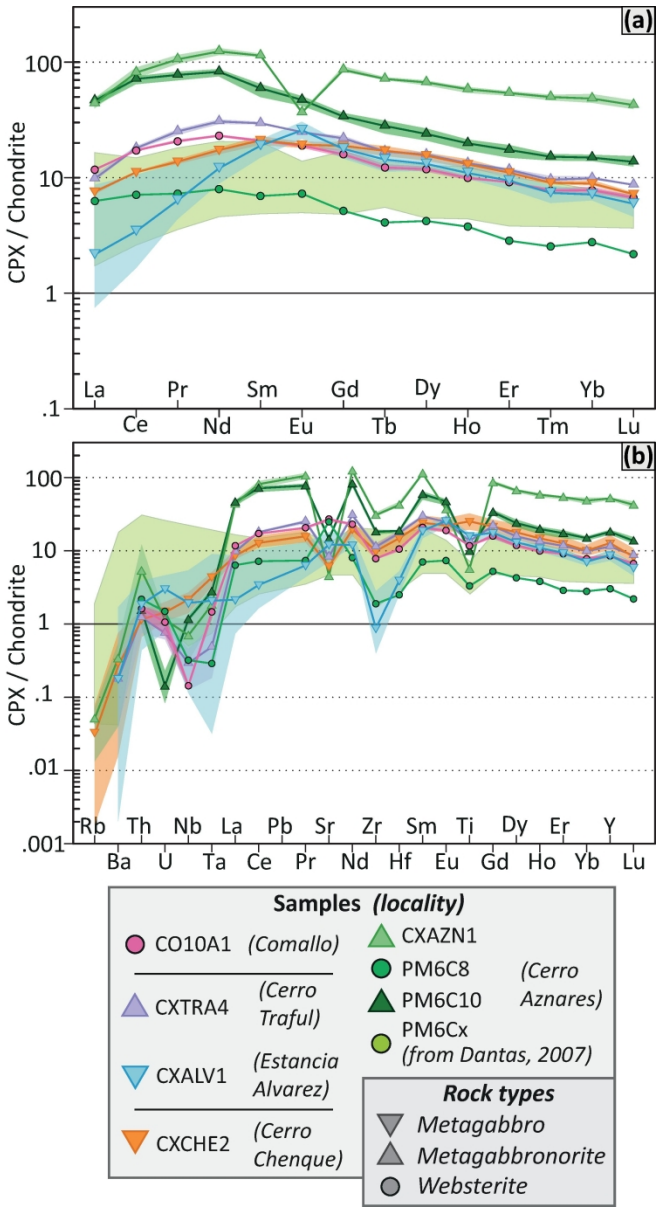

Fig. 6. Rare earth and trace elements patterns of clinopyroxene normalized to chondrite. (a) REE patterns of north Patagonian granulite xenoliths. (b) Trace elements patterns. Chondrite values are from McDonough & Sun (1995). Symbols and full lines represent analysis means while faded surfaces represent ranges of all analysis (see Table 3 for number of analyses).

103x190mm (600 x 600 DPI)

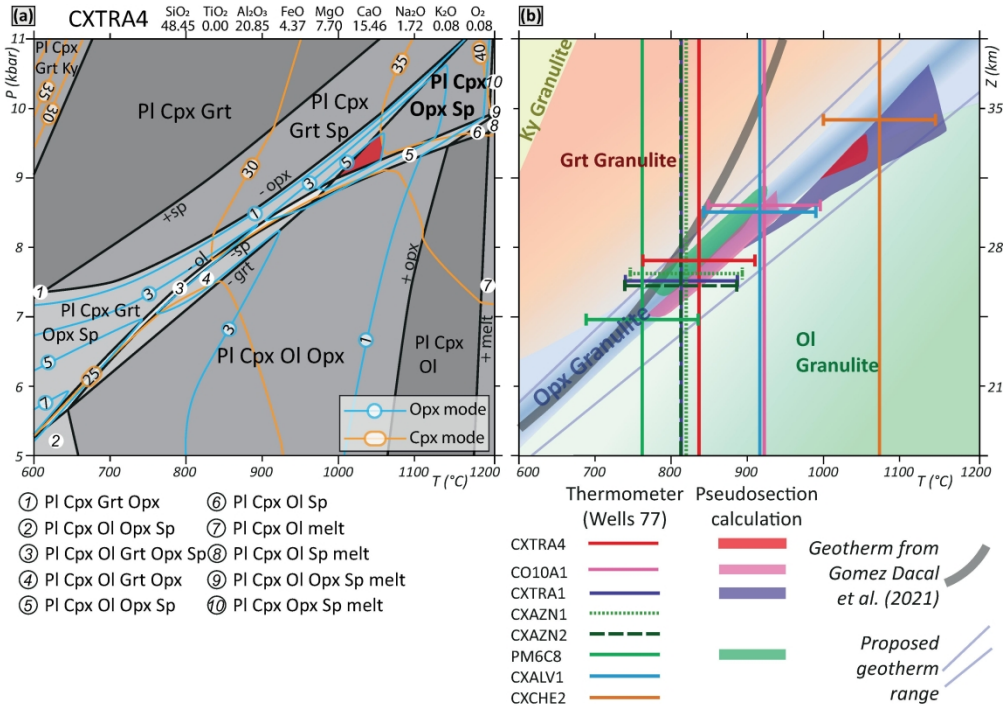

Fig. 7. Estimated temperature and pressure of granulite xenoliths. (a) Calculated P-T pseudosection for sample CXTRA4, with contoured modal proportions for orthopyroxene and clinopyroxene. As they did not add precisions to the P-T stability field determination, the plagioclase and spinel modal were not contoured to make the figure readable. (b) P-T diagram combining the results of all thermometer and pseudosection calculations. The granulite stability fields shown correspond to an average of the stability fields of all the concerned samples.

168x118mm (600 x 600 DPI)

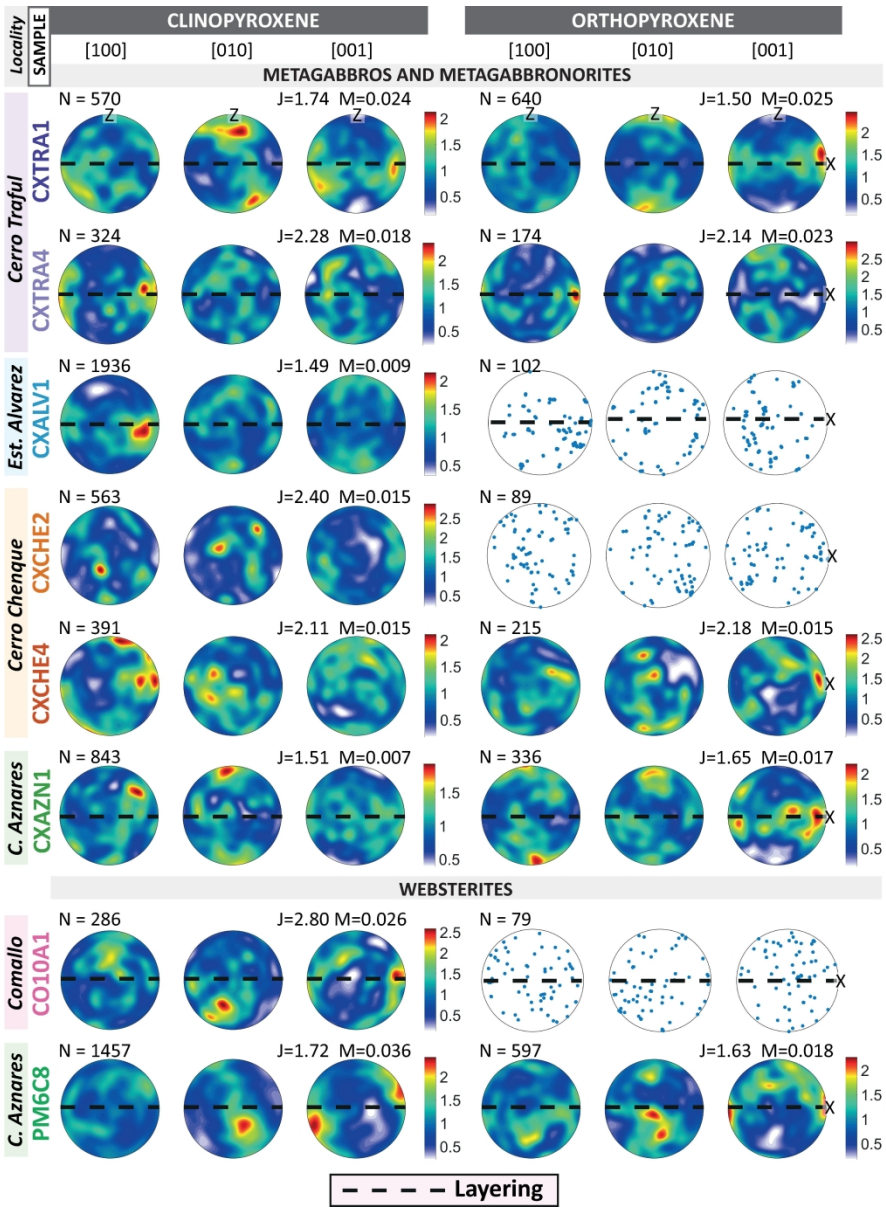

Fig. 8. Crystallographic preferred orientation of clinopyroxene and orthopyroxene of analysed metagabbros, metagabbronorites and websterites. When detected, compositional layering is tagged and pole figures are rotated as the layering normal to Z. N is the number of grains and the strength is represented by J-index and M-index. The rainbow scale represents the mud (multiply uniform density).

172x231mm (600 x 600 DPI)

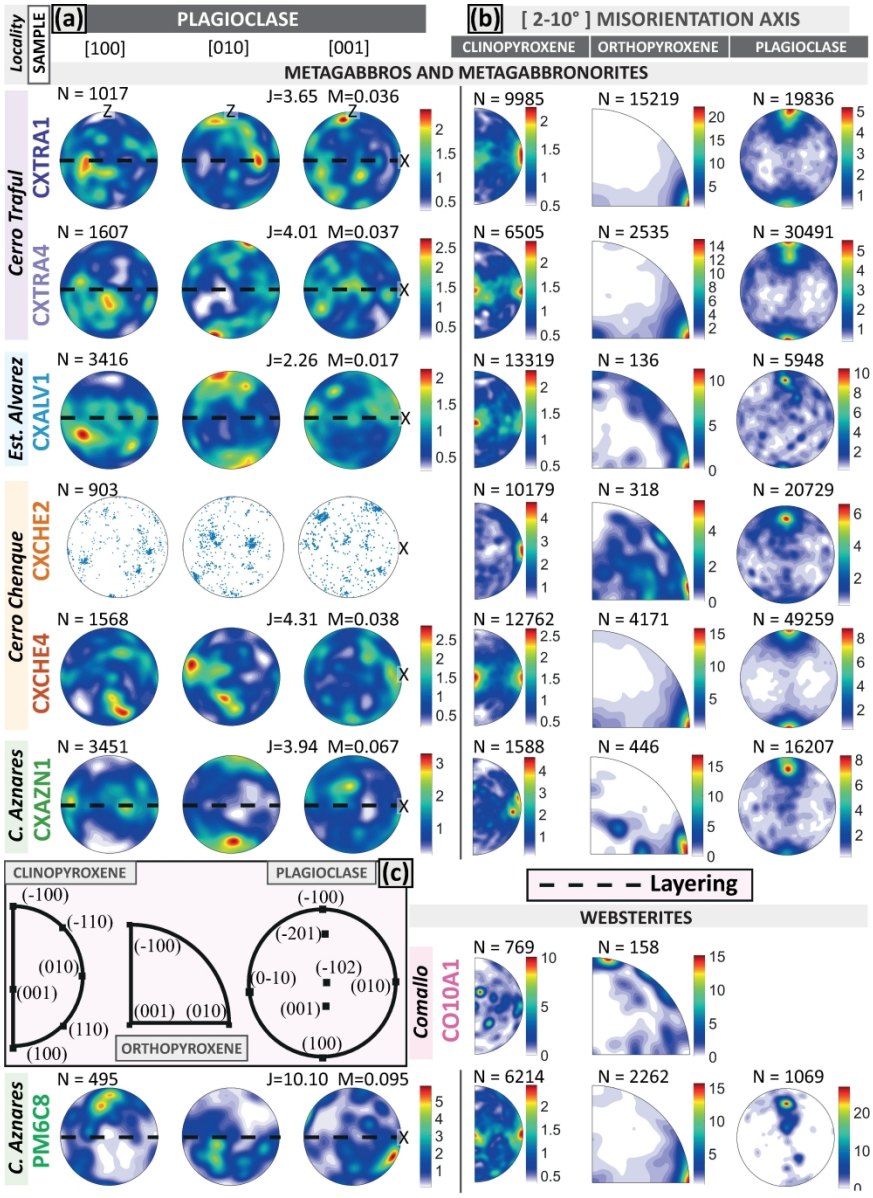

Fig. 9. (a) Crystallographic preferred orientation of plagioclase. N is the number of grains, the strength is represented by J-index and M- index. Sample CXCHE2 was not contoured because the CPO pattern is saturated by multiplied very coarse grains. (b) Rotation axes accommodating low angle (2-10°) misorientations in clinopyroxene, orthopyroxene and plagioclase grains. Data is represented in inverse pole figures where the legend can be found in (c). N is the number of pixels plotted.

176x234mm (600 x 600 DPI)

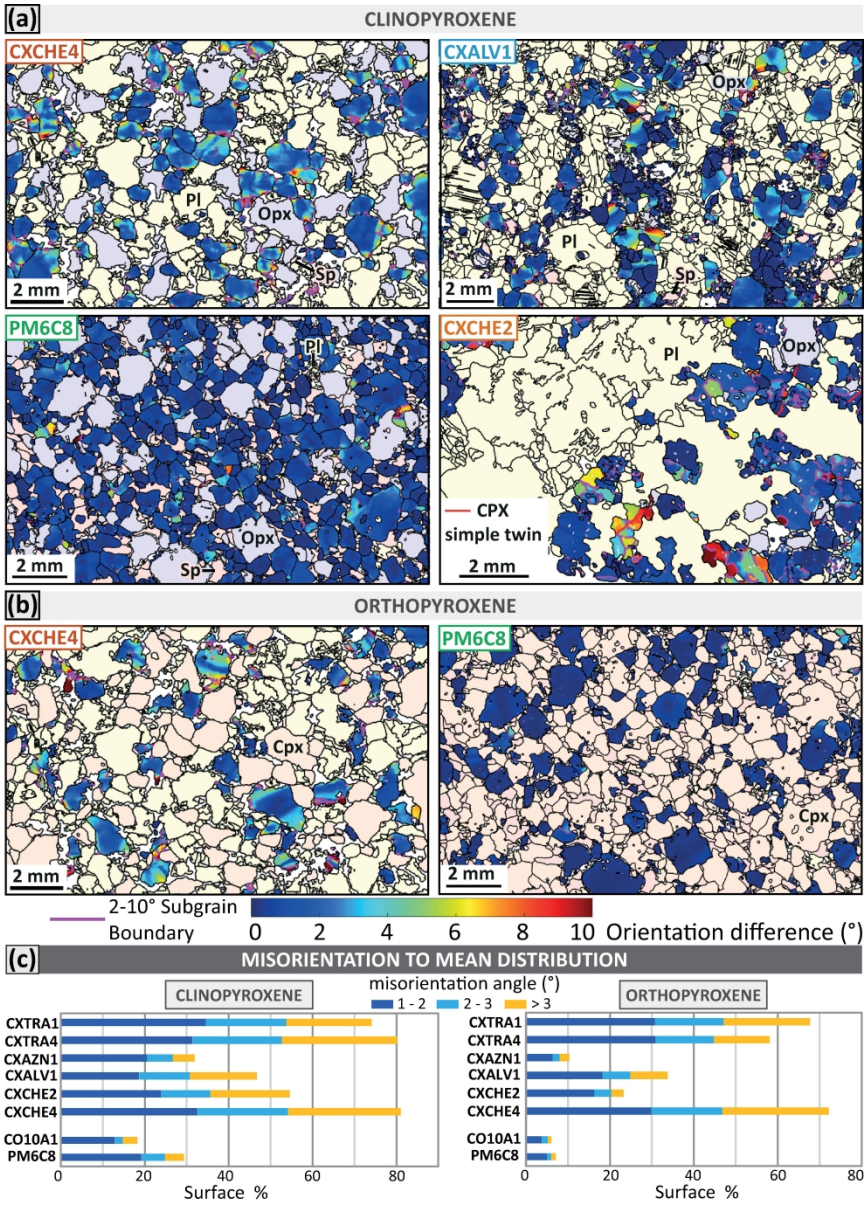

Fig. 10. Maps of intragranular deformation relative to the mean orientation of the grains for (a) clinopyroxene and (b) orthopyroxene. Deep blue grains are undeformed while the intragranular deformation is strong in green to red areas. Light blue grains are orthopyroxene, light orange is clinopyroxene, light yellow is plagioclase and light pink is spinel. (c) Normalized histograms representing clinopyroxene and orthopyroxene area proportions vs. misorientation angles (>1°) relative to mean grain orientations.

171x232mm (600 x 600 DPI)

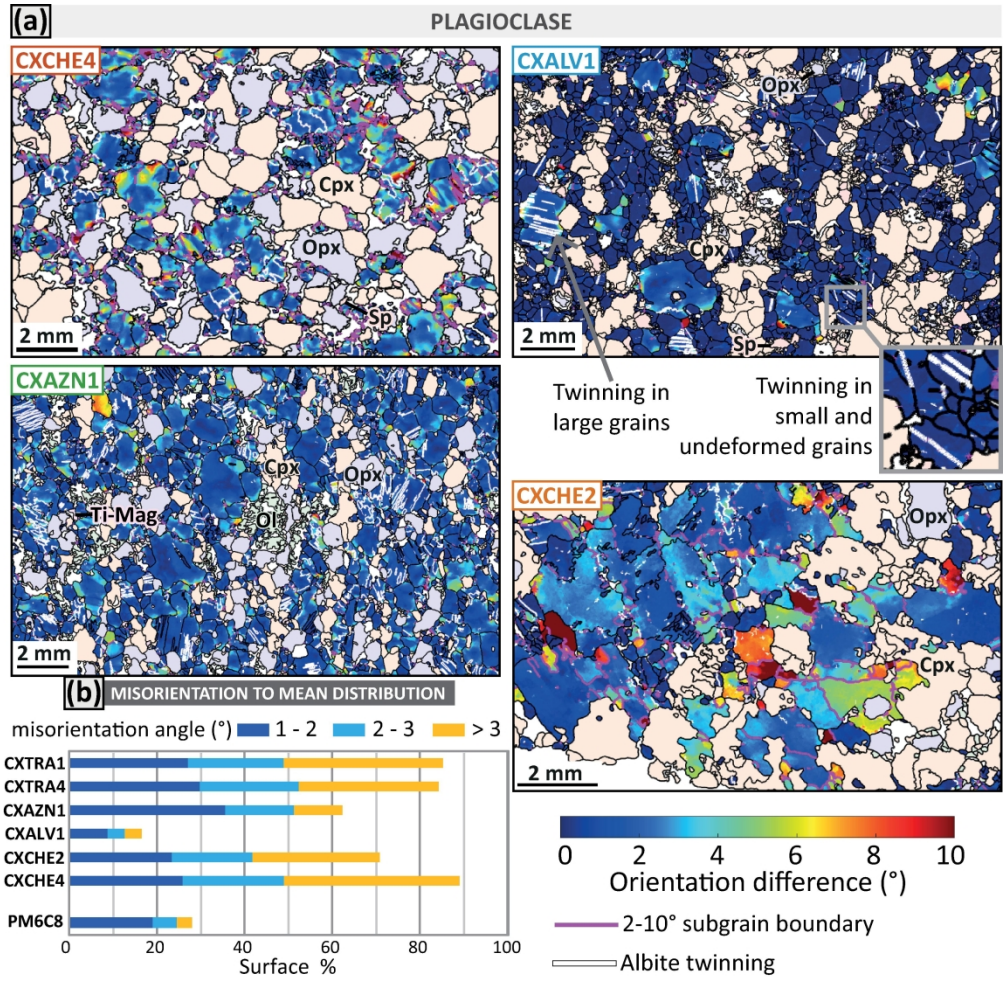

Fig. 11. (a) Plagioclase maps of intragranular deformation relative to the mean orientation of the grains. Deep blue plagioclase grains are undeformed while the intragranular deformation is strong in green to red areas. Light blue grains are orthopyroxene, light orange is clinopyroxene, light pink is spinel and light green is olivine. (b) Normalized histograms representing plagioclase area proportion vs. misorientation angles (>1°) relative to mean grain orientations.

168x164mm (600 x 600 DPI)

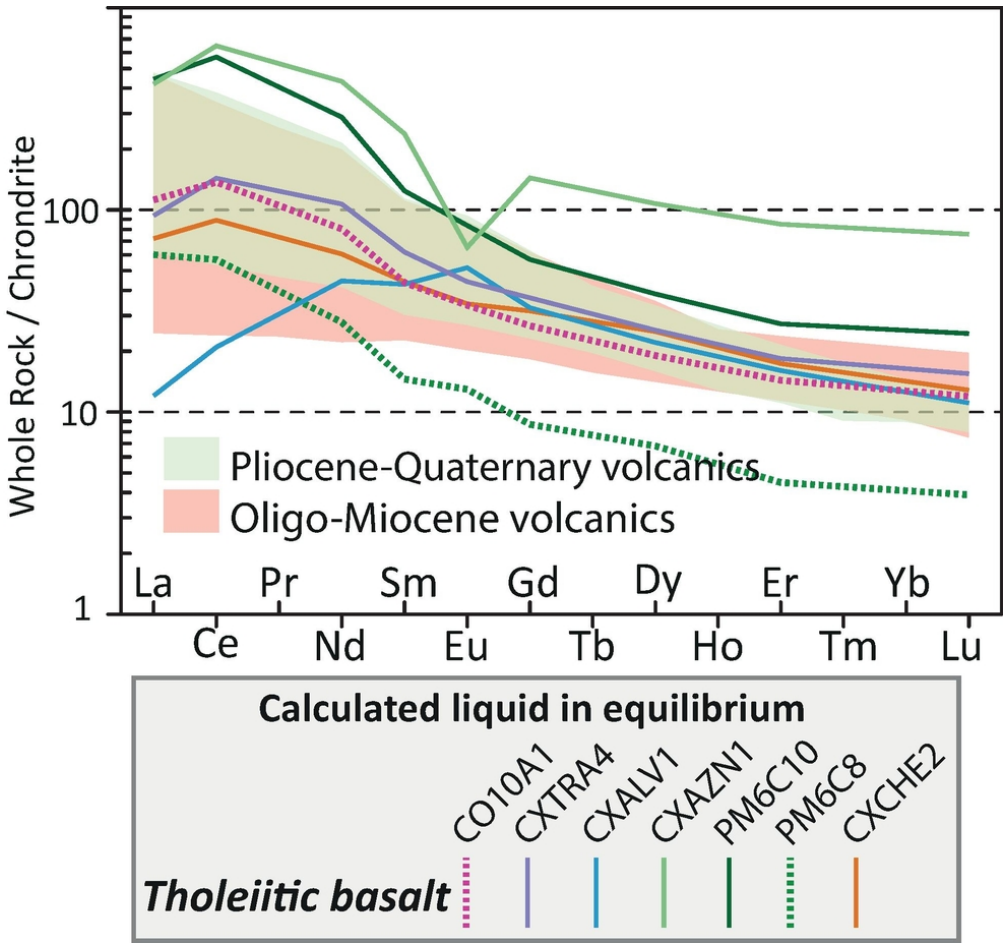

Fig. 12. Calculated normalised tholeiitic basalts in equilibrium with clinopyroxene. Oligo-Miocene and Quaternary REE volcanic compositions in the vicinity of the studied xenoliths are plotted (from Stern et al., 1990; Kay et al., 2004, 2007; Jacques et al., 2014; Massaferro et al., 2014; Asiain et al., 2022).

83x77mm (300 x 300 DPI)

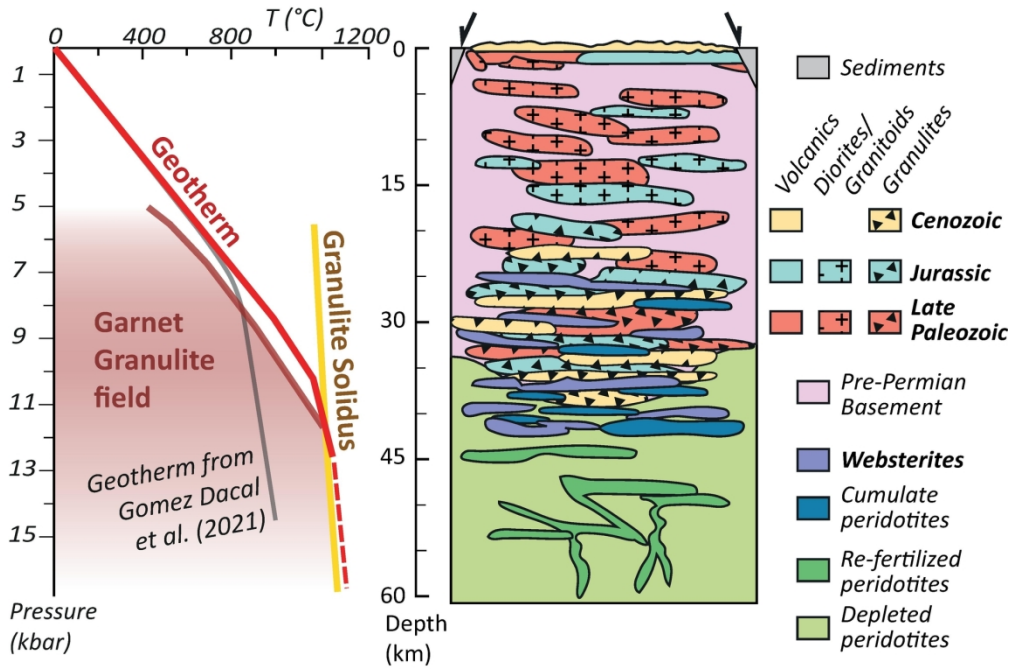

Fig. 13. (a) Estimated Cenozoic- to Quaternary-geotherm of the North Patagonian Massif and the associated lithologic section of the lithosphere between 0 and 60 km. (b) Simplified lithospheric section until 60 km in depth. The Moho is located around 32 km deep and displays an accumulation of all ages granulite lenses and websterites. The occurrence of depleted and re-fertilized peridotites and peridotite cumulates is from Mundle et al. (2016).

168x112mm (300 x 300 DPI)

Table 1: Host rock age, coordinates, modal proportions and results of the Wells (1977) thermometry of the investigated xenoliths. Modal proportions are estimated with EBSD data (with an *) or estimated (with a range of ±3%) with the optical microscope. MG: metagabbro; MGn: metagabbronorite; TiMag: titanomagnetite; Sp: spinel; W: websterite; Pl: plagioclase; Cpx: clinopyroxene; Opx: orthopyroxene; Ol: olivine; Ilm: ilmenite. We prefer for clarity to keep the mineralogical nomenclature and use the term mafic granulite. This respects the classification of Strekeisen (https://www.alexstrekeisen.it/english/meta/maficgranulite.php). For sample CXAZN1 with 72% plagioclase instead of 70% and ~27% of pyroxene and olivine instead of 30%, we round up the values.

Sample	**CO10A1***	**CXTRA1***	**CXTRA2**	**CXTRA4***	**CXALV1***	**CXCHE1**	**CXCHE2***	**CXCHE3**	**CXCHE4***	**CXAZN1***	**CXAZN2**	**PM6C8***	**PM6C10**	**PM6Cx**
Outcrop	Comallo	Cerro Traful			Est. Alvarez	Cerro Chenque				Cerro Aznares				
Host Rock Age (Ma)	*1-2*	*23-25*			*20-29*	*23-25*						*20-29*		
Latitude (°S)	40°55'	41°38'			40°46'	40°29'						40°49'		
Longitude (°O)	69°52'	69°18'			68°45'	68°44'						68°41'		
Rock type	*Sp-W*	*Sp-MGn*	*TiMag-MG*	*Sp-MGn*	*Sp-MG*	*Sp-W*	*MG*	*TiMag-MG*	*Sp-MGn*	*TiMag-MGn*	*Sp-MGn*	*Sp-W*	*Sp-MGn*	
Modal prop. (%)														
Pl	0.1	14.2	60-66	55.1	63	1-7	63.7	49-55	48.3	72	33-39	1.6	2-8	
Cpx	74.8	25.8	17-23	31.2	31.5	51-57	30.3	38-44	35.1	11.7	38-44	56	79-85	
Opx	9.45	51.5	6-12	11.2	0.8	26-32	4		12.3	12.4	11-17	29.9	2-8	
Ol	5.9	1.7	1-7	2.2			2		0.6	3.1				
Sp	9.9	7		0.3	4.7	10-16			3.7		3-9	12.5	5-11	
Ti-Mag			1-7					4-10		<0,5				
Ilm										<0,5				
T [Wells] ±70°C	920	816		836	917		1070			820	815	762		762-829

Sp-Websterite suite from Dantas (2007)

Table 2: Analysed and calculated (with an *) major elements bulk rock compositions. Rock abbreviations are the same as for Table 1.

Sample	***CO10A1****	**CXTRA1**	**CXTRA2**	**CXTRA4**	**CXALV1**	**CXCHE1**	**CXCHE2**	**CXCHE3**	**CXCHE4**	**CXAZN1**	**CXAZN2**	***PM6C8****
Outcrop	Comallo	Cerro Traful			Est. Alvarez	Cerro Chenque				Cerro Aznares		
Rock type	*Sp-W*	*Sp-MGn*	*TiMag-MG*	*Sp-MGn*	*Sp-MG*	*Sp-W*	*MG*	*TiMag-MG*	*Sp-MGn*	*TiMag-MGn*	*Sp-MGn*	*Sp-W*
wt%												
SiO2	*45.06*	46.04	49.48	47.74	47.05	44.20	51.49	46.42	46.79	52.61	44.71	*45.24*
TiO2	*0.64*	0.27	0.73	0.33	0.57	0.19	0.78	1.38	0.32	0.80	0.19	*0.16*
Al2O3	*11.41*	14.44	17.78	20.83	21.73	13.45	13.91	16.76	20.48	18.30	19.36	*13.27*
Fe2O3	*3.76*											*1.94*
FeO	*6.11*	11.39	7.79	4.86	7.21	9.21	7.82	11.46	7.48	7.72	6.99	*7.11*
MnO	*0.14*	0.17	0.13	0.08	0.09	0.14	0.14	0.14	0.11	0.13	0.10	*0.14*
MgO	*15.29*	18.03	7.88	7.80	6.10	19.04	11.12	7.47	10.01	5.80	11.22	*18.52*
CaO	*16.93*	7.23	11.44	15.37	12.22	11.73	10.11	11.77	11.05	8.36	14.72	*13.09*
Na2O	*0.66*	0.90	2.41	1.76	2.93	0.54	2.67	2.50	1.97	3.88	0.86	*0.53*
K2O	*0.01*	0.50	1.02	0.51	0.42	0.15	0.77	0.68	0.45	1.01	0.24	*0.01*
P2O5		0.05	0.03	0.03	0.04	0.02	0.10	0.06	0.04	0.19	0.02	
Total	*100.00*	100.28	99.55	99.85	99.16	99.69	99.78	99.91	99.53	99.66	99.19	*100.00*
SiO2/Al2O3	*3.95*	3.19	2.78	2.29	2.17	3.29	3.70	2.77	2.28	2.87	2.31	*3.41*
Mg#	*74.17*	73.84	64.34	61.61	60.13	78.66	71.71	53.75	70.47	57.25	74.09	*78.86*
ppm												
Nb		1.8	28.6	2.6	4.3	2	7.6	5.7	2.4	4.8	2.4	
Zr		15.5	141.3	26.7	31.2	8.5	40	38.3	25.9	46.1	15.7	
Y		3	16.8	7.4	6.4	3.7	8.8	9.2	3.8	13.4	4.5	
Sr		677.6	996.3	1073.9	1290.6	334.3	396.6	1016.1	1176	901.3	713	
Rb		10.7	37.4	16	11.5	3.6	12.1	14.7	13	10.8	6.7	
Pb		<5	5.8	<5	16.4	<5	<5	9.4	15.7	7.3	<5	
Ga		13.8	19.3	16.9	25.1	11.8	14.9	21	21.8	20.1	14.1	
Zn		96.1	77.9	64	69.6	58.4	78.6	83.2	72.3	90.7	54.7	
Cu		24.4	29.4	44.1	26	110.9	48.8	145.9	31.4	9	75.1	
Ni		241.9	50.3	42.4	23.7	198.6	194.1	65.4	121.9	52	114.7	
Co		75.2	29.2	32.3	28.9	72.3	43	44.4	43.7	32.4	44.2	
Cr		213.8	51.7	138.3	54.5	418.1	450.4	152.8	295.7	94.3	444.8	
Sc		19.9	16.6	31.9	20.1	36.4	31.3	41.9	20.9	20.6	36	
V		61.1	123.5	156.1	198.8	84.3	158.3	349.7	76.4	160	70.8	
Ce		<10	73	<10	<10	38.5	<10	<10	<10	38	<10	
Ba		375.8	694.7	631.8	246.5	1.7	112.6	500.4	374.5	524.6	52.3	
La		<10	26.5	<10	<10	<10	<10	<10	<10	16.7	<10	

Table 3: Clinopyroxene trace element compositions. n indicates the number of analyses for each sample.

	CO10A1	CXTRA4	CXALV1	CXCHE2	CXAZN1	PM6C8	PM6C10
Outcrop	Comallo	C. Traful	Est. Alvarez	C. Chenque	C. Aznares		
Rock type	*Sp-W*	*Sp-MGn*	*Sp-MG*	*MG*	*TiMag-MGn*	*Sp-W*	*Sp-MGn*
n	3	3	13	3	3	1	3
ppm							
Sc	65.7	91.0	74.4	52.6	133.9	37.1	70.8
Ti	5152	6016	7072	9673	2488	1443	4361
V	249	288	351	382	407	74	198
Co	41.3	31.3	28.8	61.9	46.2	22.8	41.8
Rb	bdl	0.01	0.31	0.07	0.12	bdl	bdl
Sr	197	60	89	39	33	1	105
Y	13	18	14	18	82	5	28
Zr	30	43	3	33	117	7	70
Nb	0.03	0.07	0.47	0.46	0.17	0.08	0.28
Ba	bdl	0.43	0.44	0.63	0.82	bdl	bdl
La	2.78	2.32	0.51	1.79	10.40	1.49	11.00
Ce	10.54	11.02	2.11	6.83	49.78	4.36	43.85
Pr	1.92	2.33	0.59	1.27	9.80	0.68	7.19
Nd	10.54	14.00	5.51	7.92	56.56	3.64	37.65
Sm	3.09	4.37	2.80	3.12	16.82	1.03	8.78
Eu	1.07	1.40	1.45	1.09	2.06	0.41	2.65
Gd	3.17	4.35	3.53	3.75	17.05	1.03	6.73
Tb	0.44	0.61	0.52	0.62	2.58	0.15	1.01
Dy	2.91	3.89	3.23	3.83	16.43	1.04	5.87
Ho	0.54	0.73	0.60	0.71	3.18	0.21	1.08
Er	1.46	1.87	1.51	1.77	8.64	0.46	2.78
Tm	0.19	0.24	0.18	0.22	1.23	0.06	0.38
Yb	1.25	1.59	1.15	1.43	7.78	0.45	2.40
Lu	0.16	0.21	0.15	0.18	1.04	0.05	0.34
Hf	1.09	1.81	0.41	1.35	4.36	0.26	1.93
Ta	0.02	0.01	0.03	0.05	0.02	0.00	0.04
Th	0.05	0.04	0.05	0.03	0.15	0.06	0.05
U	0.01	0.01	0.02	0.01	0.01	0.01	0.00
Eu/Eu*	1.0	1.0	1.4	1.0	0.4	1.2	1.1
(La/Yb)n	1.5	1.0	0.3	0.9	0.9	2.3	3.1
(La/Sm)n	0.6	0.3	0.1	0.4	0.4	0.9	0.8
(Yb/Sm)n	0.4	0.3	0.4	0.4	0.4	0.4	0.3